





PERSPECTIVE | SEPTEMBER 13 2024

Exploring the synergy between hot-electron dynamics and active plasmonics: A perspective

Special Collection: [Plasmonics and Optical Metastructures](#)

Anjan Goswami ; Andrew S. Kim ; Wenshan Cai  

 Check for updates

J. Appl. Phys. 136, 100901 (2024)

<https://doi.org/10.1063/5.0216205>



Articles You May Be Interested In

Employing surface plasmons for ultrafast nanoscale applications

Scilight (June 2023)

Preface: Special Topic on Single-Molecule Biophysics

J. Chem. Phys. (March 2018)

On Mars as it is on Earth: Bioinspired technologies for sustainability on Earth are paving the way for a new era of space exploration

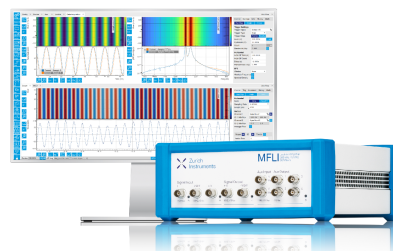
APL Mater. (February 2024)

Challenge us.

What are your needs for periodic signal detection?



[Find out more](#)



Exploring the synergy between hot-electron dynamics and active plasmonics: A perspective



Cite as: J. Appl. Phys. **136**, 100901 (2024); doi: [10.1063/5.0216205](https://doi.org/10.1063/5.0216205)
Submitted: 28 April 2024 · Accepted: 23 August 2024 ·
Published Online: 13 September 2024



Anjan Goswami,¹ Andrew S. Kim,¹ and Wenshan Cai^{1,2,a)}

AFFILIATIONS

¹School of Electrical and Computer Engineering, Georgia Institute of Technology, Atlanta, Georgia 30332, USA

²School of Materials Science and Engineering, Georgia Institute of Technology, Atlanta, Georgia 30332, USA

Note: This paper is part of the special topic, Plasmonics and Optical Metastructures.

a) Author to whom correspondence should be addressed: wcai@gatech.edu

ABSTRACT

Physical processes involving hot electrons, including their generation, transport, injection, and relaxation, have been an extensive area of research. The most widely utilized method for actuating the creation of hot electrons involves the excitation of plasmonic modes followed by their non-radiative decay, channeling the energy into these energetic carriers. Since plasmonics has already evolved into a mature field of scientific exploration, active plasmonic devices serve as an ideal platform to study hot-electron physics. In this Perspective article, we will provide the reader with a comprehensive outline of the physics underlying hot-electron dynamics. Emphasis will be placed on the characteristic timescales involved with the lifecycle of hot electrons, the generation and decay mechanisms of surface plasmon-induced hot electrons, and the material platforms suitable for such a study. Then, we will move on to discuss different temperature models used to explain the evolution of hot electrons and the changes in the optical properties of the materials they are generated in or injected into. Finally, we will focus on some of the interesting optical phenomena occurring at ultrafast timescales mediated by hot-carrier dynamics. Such a discussion is expected to incorporate valuable insights into our understanding of the synergistic relationship between hot-electron dynamics and active plasmonics, thereby paving the way for novel applications involving optoelectronics and energy conversion.

© 2024 Author(s). All article content, except where otherwise noted, is licensed under a Creative Commons Attribution (CC BY) license (<https://creativecommons.org/licenses/by/4.0/>). <https://doi.org/10.1063/5.0216205>

I. INTRODUCTION

Light-matter interaction is a rich field of scientific inquiry with dual significance, both in fundamental scientific explorations and practical applications. Such an interplay between light and matter is mediated by the exchange of energy and, as a consequence, dictated by the energy dispersion of electrons within a material. While the energy distribution of electrons within bulk materials is determined by the material type rather than their size or shape, a number of intriguing physical phenomena emerge as the material size approaches sub-wavelength dimensions, ushering in novel observations in the interaction between light and matter.

Both the physical characteristics of the incident light and the energy distribution of electrons within the material are altered through their interaction. Such changes are governed by the exchange of energy between them. The response of light includes changes in direction (transmission, reflection, and scattering), polarization (dichroism), energy (absorption), and frequency

(nonlinear optical effects). On the other hand, materials with overlapping electronic energy bands (metals) or energy bands featuring bandgaps comparable to the energy of photons in visible or near-infrared wavelengths (semiconductors) exhibit intriguing material responses. Such responses include, but are not limited to, the excitation of coherent electron oscillations known as plasmonic modes in metals and the creation of energetic electron-hole pairs in semiconductors. This simultaneous change in the physical properties of light and the energy distribution of electrons upon interaction highlights the utility of light as a sensitive probing mechanism to study the physical processes governing electron dynamics inside a material.

The generation of highly energetic electrons upon the absorption of light by a material has been a well-known physical phenomenon since the end of the nineteenth century.¹ Metals have an abundance of free electrons that can absorb energy from an incoming photon. When the energy of an incoming photon exceeds a

10 October 2024 21:53:43

threshold value known as the work function of the metal, electrons get kicked out of the metal and can be collected with the help of an externally applied potential—a physical phenomenon known as the photoelectric effect, as elucidated by Einstein.² Another intriguing observation in light-metal interaction is the generation of hot electrons, which are highly energetic charge carriers that are out of thermal equilibrium with the lattice and, as a result, do not follow the Fermi distribution at the same temperature as the lattice. Though the excitation of such highly energetic carriers by harvesting the energy of the incident light has been observed for a while now, understanding the detailed physics behind the generation, transport, injection, and subsequent relaxation is essential for practical applications. Key challenges in this pursuit include the necessity for probing techniques with high temporal resolution to monitor the ultrafast energy evolution of hot electrons with minimal disturbance, as well as the requirement to generate a significant population of hot electrons amid the abundance of free electrons in metals. Analyzing the transient changes in the characteristics of incident light—such as variations in intensity, polarization, and frequency components—upon light-matter interaction can provide significant insights into the physical processes that energetic hot carriers undergo.

Hot electrons are generated when the energy of external quantum stimuli drives electrons out of thermal equilibrium with the lattice. Right after the creation of these energetic electrons, they interact among themselves and with the lattice. These interactions facilitate their exchange of energy, eventually reaching thermal equilibrium with the lattice, typically within picoseconds. Hot electrons can be broadly classified into two different categories based on their lifetime, energy, and equilibrium status. Hot electrons that are not in thermal equilibrium among themselves cannot be described in terms of an effective electron temperature T_e . These are known as nonthermal hot electrons. These nonthermal hot electrons soon reach thermal equilibrium among themselves through electron-electron (e-e) interactions, and this occurs within a timescale of $\sim 200 - 300$ fs.³ They are now called thermalized hot electrons, which follow the Fermi distribution at an elevated electron temperature T_e , which is still far higher than the lattice temperature T_l . These thermalized hot electrons live longer than nonthermal hot electrons. Finally, they reach thermal equilibrium with the lattice primarily through electron-phonon (e-ph) interactions occurring within a timescale of 1–10 ps.^{3,4} Subsequently, phonon-phonon (ph-ph) interactions occur inside the lattice within a timescale of 10–100 ps.^{5–7}

Applications of hot electrons span various fields, ranging from chemistry to optics. A growing area of such application is photocatalysis, where the energy pathway of chemical reactions can be modified by hot carriers.^{8–10} In order to get a broad review of the application of hot electrons in photocatalysis, the readers are encouraged to consult Refs. 11–14. In addition, hot electrons can be used in photovoltaic applications since they can be injected in an efficient manner across the metal-semiconductor Schottky barrier, thanks to the lower energy requirement compared to the bandgap of semiconductors.^{15–17} Moreover, they show great promise for applications involving sensing and detection.^{18–20} A good overview of all these applications is summarized in this Perspective article.²¹ Analysis of the energy and angular

dependence of photoexcited electrons can yield significant insights into the surface properties and the electronic band structure of solids.²² Furthermore, hot electrons can be utilized for the purpose of doping semiconductors.²³ They are also used to change the phase in phase-change materials in an ultrafast manner,²⁴ which finds application in photodetection.²⁵

There are many excellent review articles on the generation of hot electrons and the relevant physics,^{5–7,26–28} temperature models for hot electrons,⁴ and the relaxation dynamics of hot electrons.²⁹ In this Perspective article, the focus will be on a set of novel optical phenomena induced by hot electrons observed in plasmonic structures on ultrafast timescales and how these phenomena can elucidate the generation, transport, injection, and relaxation of hot electrons. The first section delves into the physics of hot-electron dynamics and the ultrafast timescales involved with the physical processes taking place during the lifecycle. Then, the mechanisms behind the generation of hot electrons are discussed, including the different processes for surface plasmon decay, the choice of material combinations, the dependence of hot-electron generation efficiency on the size and shape of plasmonic nanostructures, computational models, and the relationship between computational parameters and physical observables. Subsequently, existing experimental techniques used for characterizing hot electrons are briefly discussed. A set of transient optical phenomena utilizing hot-electron dynamics are explored in Sec. III. These observations can be employed in studying the lifecycle of hot electrons, often providing new insights. Finally, a brief outlook on the future scope of research is presented.

II. UNRAVELING THE PHYSICS OF HOT-ELECTRON GENERATION AND TRANSPORT

In this section, we will explore the physics of hot electrons, focusing on their lifecycle: generation of hot electrons through different mechanisms followed by their decay through electron-electron (e-e) and electron-phonon (e-ph) collisions. Subsequently, we will explore the transport and injection of hot electrons into electron-accepting materials, which are typically semiconductors. Building upon these discussions, we will compare various popular material platforms of choice: different metals for the generation and different semiconductors for injection. Finally, we will pivot toward examining the physical alterations induced by these energetic electrons within their host materials upon generation or injection, with a special emphasis on their impact on transient changes in optical properties.

Both the generation and decay of hot carriers are inherently quantum processes. The lifecycle of hot electrons can be discussed in terms of four sequential phenomena that are well separated in a timescale. The first step involves the absorption of a photon ($\hbar\omega$) by a metallic nanostructure, followed by the coherent excitation of a charge density oscillation, with the electric field confined at the interface between the metal and dielectric, known as surface plasmon resonance (SPR). If the nanostructure is small compared to the wavelength of light, the surface plasmon resonance mode gets confined to the nanostructure, giving rise to what is known as localized surface plasmon resonance (LSPR). The decay of the plasmonic mode, which occurs within ~ 10 fs,⁷ marks the second step. Plasmonic modes decay through two channels: a radiative decay

channel, in which energy is transferred to photons,³⁰ and a non-radiative decay channel, resulting in the generation of energetic electron-hole pairs.^{31,32} These first generation of energetic electrons, known as non-thermal hot electrons, are neither in thermal equilibrium with the lattice nor among themselves. As a result, they cannot be described in terms of an effective electron temperature. The third step involves the thermalization of the non-thermal hot electrons via electron-electron (e-e) interaction, leading to the subsequent generation of thermalized hot electrons. This process occurs typically within a timescale of $\sim 200 - 300$ fs.³ These thermalized hot electrons are in thermal equilibrium among themselves and, hence, follow a Fermi distribution at an elevated electron temperature (T_e), which is higher than the lattice temperature (T_l). At this point, thermal equilibrium between the electron distribution and the lattice is yet to be established. Therefore, finally, the thermalized hot electrons undergo electron-phonon interaction, typically within a few picoseconds, to achieve equilibrium with the lattice, thereby increasing the lattice temperature (T_l) (Fig. 1).

Now, let us go through different physical mechanisms that lead to hot-electron generation. While discussing the generation mechanism of hot electrons, emphasis is placed on the processes that take place, the location, and the directionality of the generation. This will help us design structures optimized for the generation of hot electrons, followed by their ultrafast injection before they thermalize.

A. Difference between direct photoexcitation and surface plasmon decay

Two primary mechanisms for the generation of hot electrons are of particular interest: direct photoexcitation and surface plasmon decay. Hot-carrier generation by direct photoexcitation is possible in metals with a larger density of electronic states, such as d-band electrons in Au. In direct photoexcitation, a photon with energy exceeding the energy gap between the d-band and the Fermi level elevates an electron to a high-energy state. Phonons and defects take care of any momentum mismatch. For example, in the case of Au, the upper edge of the d-band is 2.3 eV below the Fermi level.³³ Hence, a photon having an energy of 3 eV can excite electrons from the d-band to a maximum of 0.7 eV above Fermi energy. On the other hand, the decay of a surface plasmon mode can provide the energy required to excite electrons into higher energy states. The key distinctions between the hot carriers produced by these two mechanisms are bipartite: (i) the energy levels of hot carriers generated via surface plasmon decay significantly exceed those from direct absorption and (ii) the excitation mechanism of a surface plasmon mode offers tremendous control through the geometry of the nanostructure and the polarization of incident light. Thus, the primary focus of this article will be on hot-carrier generation from surface plasmon decay. Before discussing the physics of SPP decay, let us briefly discuss the advantages of plasmonics in studying hot-electron physics.

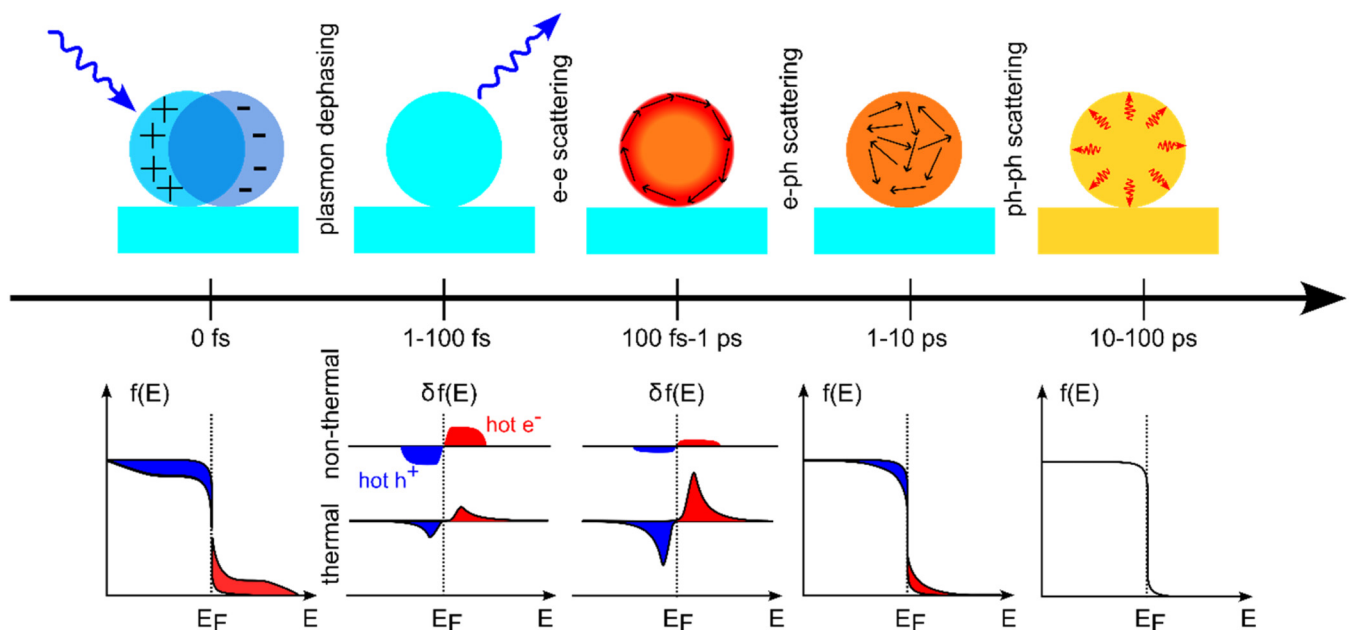


FIG. 1. Relaxation pathways and timescales following the photoexcitation of a plasmonic nanoparticle. The schematic illustrates the energy-exchange mechanisms and the corresponding characteristic timescales followed by the optical excitation of plasmonic modes in a nanoparticle. The primary energy-exchange mechanisms responsible for the transitions and the characteristic timescales involved are indicated. For each temporal region, the energy distribution of electrons $f(E)$ is presented. Contributions of non-thermal and thermal hot electrons (red) and holes (blue) around Fermi energy E_F are also pointed out for comparison.⁷ Reproduced with permission from Schirato *et al.*, *Nanophotonics* **12**, 1 (2023). Copyright 2023 Author(s), licensed under a Creative Commons Attribution 4.0 International License.

Surface plasmons are coherent, collective oscillations of conduction-band electrons in metals or any material with a negative real part of dielectric permittivity, coupled with an incident electromagnetic field, and confined to the interface between a metal and a dielectric.^{34–36} Depending on the geometric dimension of the metallic structure, surface plasmon excitation can be a propagating mode known as a surface plasmon polariton (SPP) or a localized mode known as a localized surface plasmon (LSP). Exciting the localized surface plasmon (LSP) resonance mode in metallic nanostructures, followed by their non-radiative decay, stands as the preferred method for generating hot electrons, serving both the study of underlying physics and practical applications alike. Excitation of the plasmonic modes has a number of advantages: (a) Increase in the absorption cross section: surface plasmon resonance enables metallic nanostructures to capture more light than is incident upon them.³⁷ Metallic nanostructures cause electromagnetic fields to bend toward them when in resonance, thereby augmenting the effective absorption cross section, extending even beyond geometric dimensions, and, thus, enabling efficient coupling of electromagnetic waves from free space to metallic nanostructures.^{38,39} (b) Electric field enhancement: resonant excitation of plasmonic modes can provide a large electric field enhancement.^{36,40,41} This field enhancement directly contributes to an increase in the generation of hot carriers.^{6,42} The efficacy of a hot carrier-based device hinges more on electric field enhancement than absorption efficiency. (c) Smaller mode volume: plasmonic nanoparticles can concentrate the energy of incident light on a region smaller than the diffraction limit.^{43,44} Surpassing the diffraction limit facilitates achieving a smaller mode volume.^{44–46} (d) Large number of electrons and energy levels: metals harbor a substantial number of free conduction-band electrons alongside a large number of available energy levels, easing the excitation of electrons to higher energy bands. (e) Tunability: plasmonic resonance can be tuned in an efficient manner by the physical parameters of nanoparticles (for example, size, shape, and periodicity) and incident light (for example, angle of incidence and polarization).^{47–50}

B. Hot-carrier generation from surface plasmon decay

While discussing surface plasmon decay, the physical parameters we need to look out for are the energy of hot carriers, their spatial profile, and their directionality. According to Fowler's theory,⁵¹ the law of conservation of momentum requires that only the hot carriers generated within a cone of acceptance marked by the angle θ_a in Fig. 2(a) will be able to get injected into the electron-accepting semiconductor material. For injection into an electron-accepting material, hot electrons should (a) have high energy so that they can overcome the energy barrier at the interface, (b) have a highly directional profile to have momentum toward the interface, and (c) get generated close to the interface so that they do not thermalize before injection.

For the generation of hot carriers, the following four mechanisms need to be considered.^{26,29,52}

- (i) *Interband transition mediated by direct absorption of photon* is the process where the energy of an energetic photon is utilized to elevate a d-band electron to, or slightly above, the Fermi level. Since a significant portion of the energy is

utilized to bridge the energy gap between the d-band and the Fermi level, the resulting kinetic energy of the electron above the Fermi level is typically low, often insufficient to overcome external energy barriers for injection into other materials. For example, the d-band is approximately 2 eV below the Fermi level in Au. As a result, if the energy of an incident photon $\hbar\omega$ gets absorbed by a d-band electron in Au, it can only elevate to an energy level above the Fermi level by $E_{\text{interband}} = \hbar\omega - 2$ eV. Consequently, the residual energy for the energetic interband carrier is not sufficient to perform practical work, such as surmounting a Schottky barrier for the standard illumination wavelength of interest.

- (ii) *Electron–electron scattering-assisted absorption of SPP* is neglected in some theoretical models, mainly by considering this to be a weak second order process. However, the rate of this process is on the same order as an electron–phonon (e–ph) scattering rate^{53–55} and, thus, not negligible. The scattering among energetic non-thermal electrons gives rise to the successive generation of hot carriers with lower energies. The utility of these quasi-ballistic carriers depends on the number of e–e scattering events they have undergone and the energy barrier they are required to overcome during an application. Two hot electrons and two hot holes are generated in one such scattering event with an equal distribution of energy. Thus, the energy of each charge carrier is $\hbar\omega/4$ and the spatial profile of the generation is omnidirectional, given by $R(\theta_a) = \frac{1}{4\pi}$.⁵² Thus, the lack of directionality also hinders their application.
- (iii) *Phonon and defect-assisted absorption of SPP* is the process of SPP decay that involves a phonon or a defect to compensate for the momentum mismatch. The energy of the SPP mode is split evenly between an electron–hole pair, with each having an average energy of $\hbar\omega/2$. The directionality is weak, and the directional profile is given by $R(\theta_a) = (3\cos^2\theta_a + 1)/8$.⁵²
- (iv) *Landau or surface collision assisted damping of SPP* is the damping process of the SPP mode near the end of the surface, where the conservation of momentum is relaxed.^{56,57} This is by far the most useful process for hot-carrier generation since the generated hot carriers are both energetic with an average energy of $\hbar\omega/2$ and highly directional with the directional profile $R(\theta_a) = \frac{\cos^2\theta_a}{\pi}$.⁵² Additionally, these are generated close to the surface from where they can be easily injected.

A comparison of all the decay mechanisms is shown in Table I based on the theoretical model presented in Ref. 52.

The injection of hot carriers was initially described by Fowler theory⁵¹ where only those hot carriers having a momentum within the cone of acceptance can be injected into the semiconductor [Fig. 2(a)]. Various hot-carrier generation mechanisms differ in their directionality and injection efficiency [Fig. 2(b)]. Among the generation mechanisms, a surface collision assisted or Landau damping assisted mechanism is the most efficient one in terms of injection since most of the hot carriers are generated within the mean free path L_{mfp} of the surface [Fig. 2(c)]. The flux and, hence, the internal quantum efficiency (IQE) of hot-carrier injection

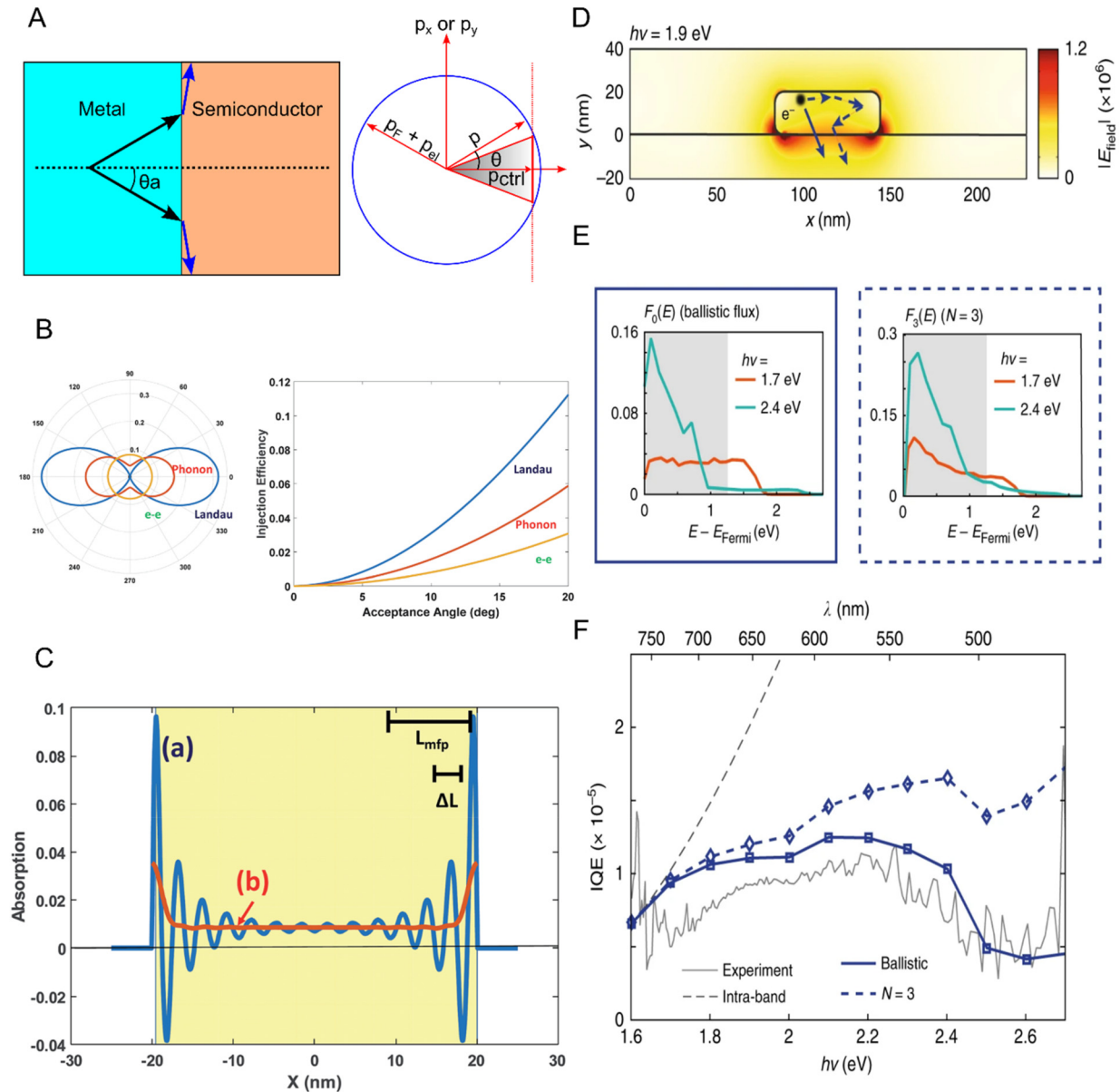


FIG. 2. Hot-carrier generation and injection. (a) Spatial picture of a metal–semiconductor Schottky barrier with angle of acceptance θ_a for allowed injection (left)⁵² and a schematic showing an isotropic hot-electron momentum distribution in a sphere and a limited escape cone (right).⁵⁸ (b) Angular distributions of hot carriers photoexcited by different processes (left) and injection efficiency of the hot carriers excited by each process (right).⁵² (c) Spatial dependence of the energy dissipation rate in a 40 nm thick Au plate [blue curve marked as (a)] and the same as the blue curve but with the oscillations smoothed out over each period [red curve marked as (b)].⁵² (d) Computed spatial profile of the norm of the electric field $|E_{\text{field}}|$ at the resonance wavelength ($\lambda = 650$ nm) for an experimental structure with $W = 61$ nm and $P = 230$ nm. The hot electrons travel across the metal structure and reach the interface between Au and GaN either ballistically (without scattering, solid arrow) or after scattering (dashed arrows).⁵⁹ (e) Energy-resolved flux of hot electrons reaching the Au–GaN interface ballistically for a photon energy of 1.7 eV (corresponding to a weak interband contribution, orange curves) and 2.4 eV (corresponding to a strong interband contribution, turquoise curves). The position of the Schottky barrier is shown by the shaded area (left), the same as the left panel but considering the flux of carriers that have experienced at most three scattering events (right).⁵⁹ (f) Internal quantum efficiency (IQE) spectra computed using the energy-resolved fluxes, both for the cases of ballistic carriers (blue solid curve) and for carriers that have gone through three scattering events (blue dashed curve).⁵⁹ Tangential momentum conservation was assumed for injection probability.¹⁸ Figure panels (a) (left), (b), and (c) are reproduced with permission from Khurgin *et al.*, *Faraday Discuss.* **214**, 35 (2019). Copyright 2019 The Royal Society of Chemistry. Figure panel (a) (right) is reproduced with permission from Leenheer *et al.*, *J. Appl. Phys.* **115**, 134301 (2014). Copyright 2014 AIP Publishing LLC. Figure panels (d)–(f) are reproduced with permission from Tagliabue *et al.*, *Nat. Commun.* **9**, 3394 (2018). Copyright 2018 Author(s), licensed under a Creative Commons Attribution 4.0 International License.

TABLE I. Comparison among the SPP decay mechanisms.

SPP decay mechanism	Average energy of hot carriers	Directionality	Location of hot-carrier generation
Electron–electron scattering	$\frac{\hbar\omega}{4}$	No, $R(\theta_a) = \frac{1}{4\pi}$	Entire SPP mode
Phonon or defect-assisted	$\frac{\hbar\omega}{2}$	Low, $R(\theta_a) = (3\cos^2\theta_a + 1)/8$	Entire SPP mode
Landau damping	$\frac{\hbar\omega}{2}$	High, $R(\theta_a) = \frac{\cos^2\theta_a}{\pi}$	Surface of the metallic structure

depend on the nature of the hot carriers. Ballistic carriers that have not undergone any e–e scattering are compared with the hot carriers that have undergone three such e–e scattering events. This is shown for an experimental Schottky junction made of Au–GaN [Fig. 2(d)]. As illustrated in Fig. 2(d), upon excitation of the fundamental plasmon mode, the electric field becomes localized near the metal–semiconductor interface. Figure 2(e) illustrates the impact of strong interband transitions, as shown by the turquoise curve, for both cases: the ballistic flux $F_0(E)$ on the left panel and the flux of carriers that have experienced three scattering events $F_3(E)$ on the right panel, in contrast to the weak interband transitions indicated by the orange curve. The gray dashed curve in Fig. 2(f) depicts the predicted IQE based on the fit of the Fowler yield, exhibiting little resemblance to the experimentally observed IQE represented by the solid gray curve. The blue solid curve depicts the IQE spectrum projected from the flux of hot electrons without undergoing any scattering, denoted as $F_0(E)$. Meanwhile, the blue dashed curve represents the predicted IQE obtained for hot electrons that have experienced three scattering events, labeled as $F_3(E)$. The inclusion of additional scattering events has been shown to marginally alter the IQE by 0.01%, suggesting that most hot electrons undergo no more than three scattering events before being collected.

Now, based on our understanding of the physics behind different hot-electron generation schemes, a number of design principles can be established to fine-tune the process.

- (i) Efficient absorption of light by the excitation of the localized surface plasmon mode: the first step toward the generation of hot electrons is the absorption of light and hence comes to the use of metallic nanostructures. Though bulk metal structures are mostly reflective, metallic nanostructures can provide a high absorption cross section beyond their geometric dimension thanks to the excitation of an LSP mode.³⁷ Again, a recent progress in nanofabrication techniques has enabled the fabrication of complex metallic nanostructures that are intentionally designed for efficient absorption of photons.^{60,61}
- (ii) Non-radiative decay of surface plasmon: only the non-radiative decay of surface plasmons contributes to the generation of hot electrons. Radiative decay, on the other hand, leads to the emission of photons. Therefore, the non-radiative decay channel needs to be prioritized over the radiative one, and this can be accomplished through approaches involving the excitation of a dark plasmon mode,⁶² activation of a propagating surface plasmon mode,⁶³ and taking advantage of surface and geometric effects,⁶⁴ among others.
- (iii) *Landau damping*: Landau damping is a surface scattering-assisted decay mechanism for surface plasmons.

Hot electrons generated through Landau damping are valuable for practical applications thanks to their higher energy, high directionality, and the fact that their generation site is close to the surface. Enhancing the surface-to-volume ratio increases the generation of hot electrons through Landau damping.⁶⁴

C. Generation and injection of hot holes for modulating hot-electron dynamics

Though the injection of hot electrons from plasmonic nanostructures into an electron-accepting material has been under thorough investigation, the injection of hot holes has not been studied extensively. The generation of hot holes created below the Fermi level of metallic nanostructures, followed by their collection into the valence band of a hole accepting material, leads to substantial modulation of the relaxation dynamics of hot electrons. This alteration is observed in terms of an increase in the maximum electron temperature (T_e), which further leads to an elevated electronic heat capacity (C_e). Moreover, electron–phonon coupling time (τ_{e-ph}) is observed to decrease as well.⁶⁵ The difference in the spectral signature of hot hole dynamics compared to hot-electron dynamics plays a critical role in selecting the suitable spectral content for both the pump and the probe beam. Hot holes excited from the d-band of the metallic nanostructures are suitable for modulating the hot-electron dynamics and, as a result, require the use of pump photons energetic enough to realize an interband transition. On the other hand, the relaxation dynamics of hot holes can be studied using near-IR or mid-IR probe light.⁶⁶ This difference in the spectral region of interest for studying hot-electron dynamics and hot hole dynamics makes it easier to study them independently of each other.

D. Importance of a pulsed laser

Excitation of a SPP mode can concentrate the energy of the incident light in a small mode volume, which is well beyond the diffraction limit governed by the wavelength of the incident light. This, along with the fact that they have a short lifetime, typically in the range of ~ 10 fs, leads to the requirement of a very large incident power density, sometimes even beyond 1 MW/cm^2 in the case of a resonant nanostructure of sub-wavelength dimensions.²⁹ The short lifetimes of hot carriers, in comparison with the successive excitation of SPP modes, make it highly improbable for a temporal overlap between an SPP mode and hot energetic carriers in a nanostructure. In most practical cases of irradiation, there exists either an SPP mode, a pair of energetic carriers, or, more likely, none of these inside the nanostructure. Consequently, many experimental

studies examining hot-carrier generation from surface plasmon decay necessitate the use of pulsed lasers with low repetition rates, thus generating a high peak power.^{54,55}

For a pulsed laser with an average power of P_{avg} , the energy in each pulse can be calculated using the repetition rate R (i.e., the number of laser pulses in each second) as shown in Eq. (1),

$$E_{\text{pulse}} = \frac{P_{\text{avg}}}{R}. \quad (1)$$

Therefore, the lower the repetition rate of the pulsed laser, the higher the energy contained in each pulse of the laser. For example, if two pulsed lasers have the same average power, if one of them has a repetition rate of 1 KHz while the other has a repetition rate of 1 MHz, then each optical pulse in the first laser will have 1000 times more energy than each pulse in the second laser. The higher the energy contained in each pulse, the higher the probability of exciting a non-equilibrium electron. Hence, the utilization of femtosecond pulsed lasers serves several crucial purposes: they provide peak power that is sufficient for exciting energetic hot carriers, maintain a reasonable average power thanks to their low repetition rate, which prevents excessive heat accumulation and consequent melting of metallic nanostructures, and offer the requisite temporal resolution for investigating the ultrafast dynamics of hot carriers.

E. Material choices

Most applications involving hot electrons entail the injection of these energetic carriers into an electron-accepting material, typically a semiconductor that forms a Schottky barrier with the metallic structure generating hot electrons. The short mean free path and the ultrafast relaxation of hot carriers make it challenging to collect them into the electron-accepting material before they thermalize. The collection of hot carriers is a two-step process. At first, they need to travel to the metal–semiconductor interface without decaying, and then they need to overcome the Schottky barrier to get injected into the semiconductor. The injection efficiency depends on a few factors: (a) location of the hot-carrier generation, (b) conservation of linear momentum at the interface, (c) height of the metal–semiconductor Schottky barrier, (d) density of states (DOS) available in the electron-accepting material, and (e) the effect of interface roughness, among others. The closer the hot carrier is generated to the interface, the higher the chance it gets injected before being thermalized. The conservation of linear momentum is relaxed at a rough interface. This relaxed momentum conservation results in a higher efficiency of hot-carrier extraction into the semiconductor. The height of the Schottky barrier also has an impact on carrier injection since the carrier should have sufficient energy to overcome this barrier in the first place. The higher the Schottky barrier, the lower the probability of a carrier crossing it. Finally, a higher density of states in electron-accepting materials favors the injection of electrons. For example, owing to the low density of states in Si, the efficiency of hot-electron injection from Au to Si is typically on the lower side.⁶⁷ On the contrary, the injection efficiency from Au to TiO₂ can be very large and can even surpass 10%.¹⁴

The energy distribution of hot electrons is intricately linked to the electronic band structure of the metal. For example, when

metallic structures composed of materials, such as Au and Cu, are excited, they yield hot electrons with temperatures typically 1–2 eV higher than that of hot holes. In contrast, materials, such as Ag and Al, evenly distribute energy between hot electrons and hot holes. This results from the fact that the momentum-direction distributions for hot carriers are anisotropic and dominated by crystal orientation for noble metals.

The energy distribution of hot carriers is connected to the electronic band structure of the metal in an intricate manner. For example, when metallic nanostructures composed of Au and Cu are excited, they yield hot electrons with temperatures typically corresponding to 1–2 eV higher energies than those of hot holes. In contrast, an even distribution of energy between hot electrons and hot holes is observed in materials, such as Ag and Al. This originates from the anisotropy in the momentum-direction distributions for hot carriers, which is dominated by the crystal orientation in noble metals.

The initial hot-carrier distribution generated by plasmon decay has been estimated using jellium models, which are based on the free-electron band structure, specifically for Ag nanoparticles and nanoshells.⁶⁸ Despite providing valuable insights into the physics of plasmonic hot-carrier generation, these models are applicable to cases for materials and ranges of plasmon energies that only involve free-electron-like potential distribution. For instance, this approach is valid for Ag nanoparticles below its interband transition threshold of 3.6 eV, but not applicable to other metals, such as Au, Cu, or Al, since they exhibit interband transitions at lower energies.

In addition, the selection of the metal–semiconductor combination depends on the intended application since the overall efficiency of hot-carrier injection is influenced by the Schottky barrier formed at the interface. Figure 3(a) summarizes popular material selections, including metals, conducting oxides, and wide-bandgap semiconductors, utilized for the generation and collection of plasmonic hot electrons, accompanied by their respective energy band characteristics. The efficiency of hot-carrier generation also depends strongly on the size and shape of the unit cells of the plasmonic structure. These effects are studied in Ref. 69 for four different geometric shapes (sphere, nanorod, nanostar#1, and nanostar#2) and different sizes [Fig. 3(b)]. Among these shapes, the nanostar exhibited the highest efficiency in generating hot electrons [Figs. 3(c)–3(e)]. This is primarily attributed to several factors, including the strong plasmonic enhancement of the internal field, the presence of localized hot spots, an increased surface-to-volume ratio, the nearly isotropic optoelectronic properties, as well as the lack of interband transitions at the plasmonic resonance frequency.⁶⁹

F. Computational methods

Several computational methods are used to design and analyze the spatial profile of the electric field in the plasmonic nanostructure upon the incidence of light. Full wave electrodynamic simulation methods serve as excellent tools for such calculations. The temporal evolution of non-equilibrium carriers is modeled using density functional theory (DFT) and temperature models (TMs).

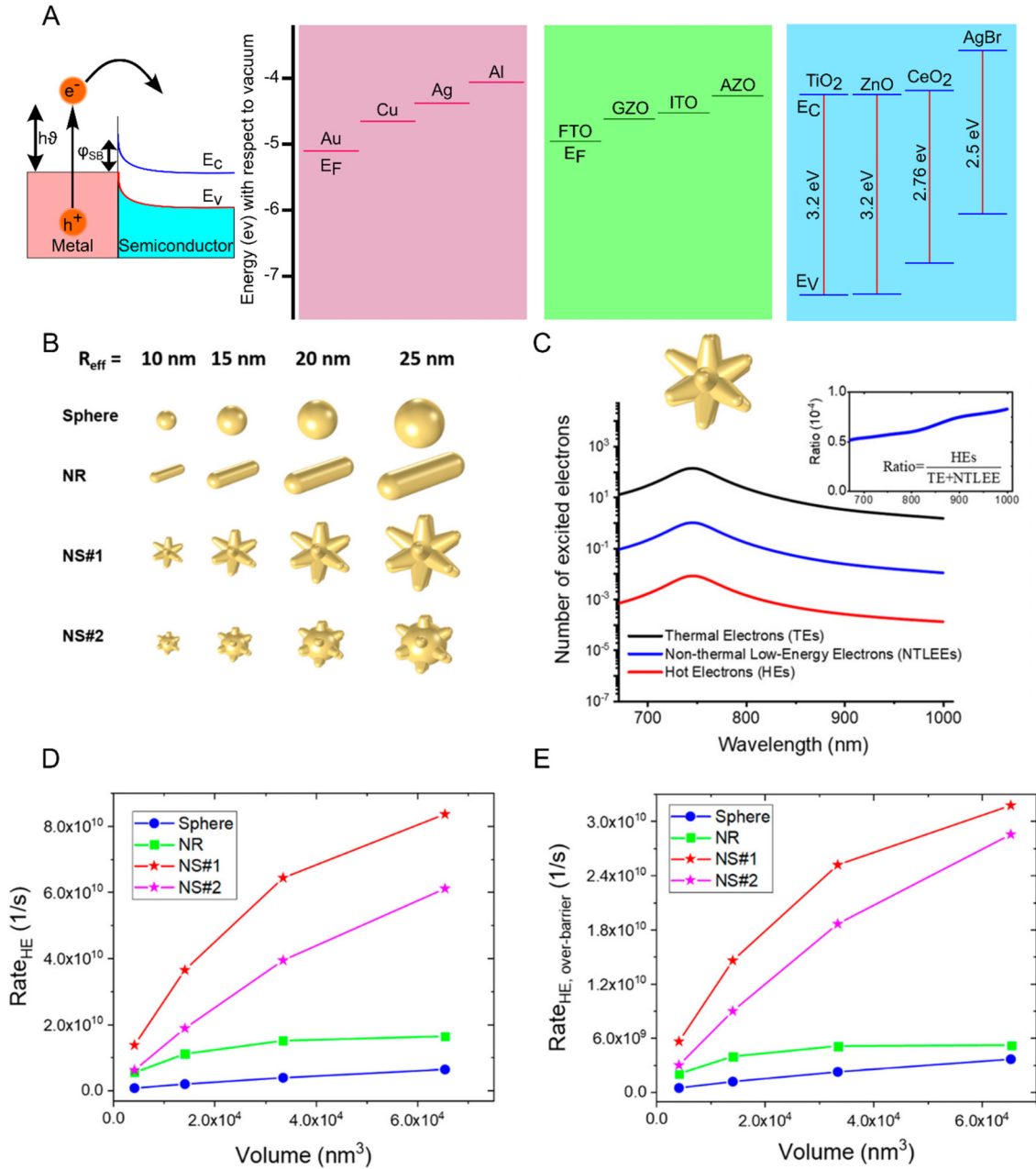


FIG. 3. Choice of material combinations, size, and shape for efficient hot-carrier generation. (a) Schematic of the energy band diagram of a metal–semiconductor Schottky junction. The absorption of a photon $h\nu$ causes the creation of an electron–hole pair that can overcome the Schottky barrier ϕ_{SB} (left). Fermi level (E_F), conduction (E_C), band, and valence (E_V) band energy for a few metals, conducting oxides, and wide-bandgap semiconductors, which are of interest for the fabrication of plasmonic nanostructures. A potential scale (V) is used to plot the energies with respect to the vacuum (right).⁵ (b) Different shapes and sizes of nanoparticles under study. The nanorods (NRs) have the same aspect ratio of 3.5.⁶⁹ (c) The number of photoexcited electrons in the nanostar as a function of the wavelength around the plasmonic resonance of $\lambda_p = 745$ nm. Inset: the ratio between the number of hot electrons and the number of electrons with low excitation energies.⁶⁹ (d) Rates of intraband generations as a function of nanocrystal volume for all different shapes of nanostructures.⁶⁹ (e) Rates of intraband generations as a function of nanocrystal volume for the over-barrier carriers.⁶⁹ The E_F values for Au, Cu, Ag, Al, FTO, GZO, ITO, and AZO were obtained from Refs. 70–77, respectively. The values of E_C and E_V for TiO₂, ZnO, CeO₂, and AgBr were obtained from Refs. 78–81, respectively. Figure panel (a) is reproduced with permission from C. Clavero, Nat. Photonics 8, 95 (2014). Copyright 2014 Springer Nature Limited. Figure panels (b)–(e) are reproduced with permission from Santiago *et al.*, ACS Photonics 7, 2807 (2020). Copyright 2020 American Chemical Society.

1. Full wave electrodynamic simulation

Since the dawn of plasmonics, full wave electrodynamic simulation has been used for numerical analysis and design of plasmonic structures. Such electrodynamic simulations are mostly performed using (i) a Finite Element Method (FEM) and (ii) Finite Difference Time Domain (FDTD) analysis. A rationally designed electrodynamic simulation is performed to calculate (i) transmittance and reflectance spectra and (ii) the spatial profile of the electric field. Electric field enhancement is correlated with plasmonic resonance, which, in turn, can be predicted using the transmittance and reflectance spectra. The spatial profile of hot-electron generation $\delta n(E, r)$ is directly related to the electric field profile by the following quadratic relation:⁸²

$$\delta n(E, r) \propto |E(r)|^2. \quad (2)$$

This correspondence between the spatial distribution of hot-electron generation and electric field enhancement is utilized while designing plasmonic platforms for the study of hot electrons.

2. Density functional theory (DFT)

A comprehensive examination of hot-carrier dynamics within a metallic nanostructure requires the application of time-dependent density functional theory (TD-DFT).^{83–85} Leveraging TD-DFT, carrier density of states, and optical transition matrix elements can be determined without using free parameters. TD-DFT also serves as a distinctive tool for many purposes: probing photoinduced charge transfer mechanisms occurring at the plasmonic nanoparticle (NP) surface,⁸⁶ validating experimental findings of ballistic thermal injection at metal/semiconductor interfaces,⁸⁷ elucidating ultrafast electron transfer dynamics within heterostructures⁸⁸ and 2D materials,⁸⁹ and providing insights into the impact of plasmons on photocatalysis. However, the problem TD-DFT suffers from is the numerical complexity, which grows exponentially with the dimension of the system under study. As a result, TD-DFT is suitable only for systems comprising a few hundred atoms with physical dimensions of 1–2 nm. Modifications within TD-DFT based on reasonable assumptions result in reduced computational complexity, thereby facilitating its application in systems with more realistic dimensions. Utilization of analytical free-electron solutions and jellium TD-DFT, as alternatives to full band calculations,^{90,91} extends their applicability to nanostructures spanning tens of nanometers. Such computations offer valuable insights into phenomena, such as geometry-assisted transitions and the influence of nanostructure shapes.⁹² Hybrid computational solutions, derived from the Boltzmann equation (BE), have also been shown to capture the interesting features of diffusive transport.⁹³ Apart from the complexities inside the models themselves, there is also technical difficulty in incorporating these models with the commercial full wave solvers typically used to design the metallic structures for plasmonic resonance.

3. Temperature models

In addition to the advanced techniques previously discussed, there are thermodynamic-based models that provide effective

descriptions of hot-electron dynamics. These models encompass the two-temperature model (2TM),⁹⁴ the extended two-temperature model (e-2TM),⁹⁵ the quantum two-temperature model (Q-2TM),⁹⁶ the three-temperature model (3TM),⁹⁷ and the four-temperature model (4TM).⁹⁸ The 2TM approach treats the dynamics of photoexcited carriers as the thermalization process of two interlinked thermal reservoirs: hot electrons at an elevated temperature T_e and the lattice at a temperature T_l . These variables are interconnected through rate equations and the principle of energy conservation. 2TM successfully captures the thermal non-equilibrium between the hot-electron distribution and the lattice. However, a notable limitation of the 2TM is its failure to account for the thermal non-equilibrium among the hot electrons themselves immediately following their creation. This early phase of the hot-electron lifecycle, characterized by electron–electron scattering, eludes the scope of the 2TM model.

A slightly modified version of 2TM is the e-2TM. In this model, the non-thermal hot electrons excited right after the decay of an LSP mode are taken into account. The thermalized hot electrons are modeled by an elevated electron temperature T_e , and the lattice temperature is denoted by lattice temperature T_l . The non-thermal hot electrons cannot be modeled by temperature. Hence, they are modeled by the energy content of the nonthermal electron distribution E_{nth} . The model describes the relationship among these three quantities T_e , T_l , and E_{nth} in terms of three coupled differential equations.

The overall process starts from the absorption of energy from LSP decay $P_{abs}(t)$, which creates a non-thermal hot-electron distribution with energy E_{nth} . These non-thermal hot electrons thermalize by e–e scattering, with the scattering coefficient denoted by a_{e-e} . This process takes place at ~ 200 fs timescale. The rate of scattering is proportional to the initial population of non-thermal hot electrons. This gives rise to the following differential equation for the decay of non-thermal electrons:⁹⁹

$$\frac{dE_{nth}}{dt} = P_{abs}(t) - a_{e-e}E_{nth}. \quad (3)$$

Once an equilibrium is reached within the hot electrons, they follow the Fermi distribution at an elevated temperature T_e , known as the electron temperature, which is greater than the lattice temperature T_l . Now, there is a transfer of energy from the non-thermal hot electrons when they thermalize, given by $a_{e-e}E_{nth}$, and there is a thermalization process dominated by the e–ph scattering between the thermalized electrons and the lattice. This electron–phonon coupling coefficient is given by G . Therefore, we get the following differential equation for the thermalized hot-electron distribution:⁹⁹

$$C_e \frac{dT_e}{dt} = a_{e-e}E_{nth} - G(T_e - T_l). \quad (4)$$

Here, C_e denotes the heat capacity of the electron distribution, which is proportional to the electron temperature T_e . Finally, the lattice at temperature T_l absorbs energy from the thermalized hot electrons by e–ph interactions, and they eventually radiate heat to the external environment. This gives rise to the following

differential equation for the lattice:⁹⁹

$$C_l \frac{dT_l}{dt} = G(T_e - T_l) - C_l \frac{T_l - T_0}{\tau_{\text{heat transfer}}}. \quad (5)$$

Here, C_l denotes the lattice heat capacity and $C_l \gg C_e$. $\tau_{\text{heat transfer}}$ represents the time required for heat transfer from the plasmonic nanostructure to the surrounding medium.

Another temperature model close to the e-2TM is 3TM. 3TM accounts for the photogeneration and ultrafast relaxation of hot carriers in terms of the same three internal energetic degrees of freedom. While the designation “3TM” may be somewhat misleading, as it implies the introduction of an additional temperature, the model accurately represents the non-thermal hot electrons in terms of the energy density stored in the non-thermalized portion of the distribution E_{nth} , as these hot electrons cannot be modeled using an effective electron temperature.

3TM reads as the following set of coupled ordinary differential equations:⁹⁷

$$\frac{dE_{nth}}{dt} = P_{abs}(t) - a_{e-e}E_{nth} - b_{e-ph}E_{nth}, \quad (6)$$

$$C_e \frac{dT_e}{dt} = a_{e-e}E_{nth} - G(T_e - T_l), \quad (7)$$

$$C_l \frac{dT_l}{dt} = b_{e-ph}E_{nth} + G(T_e - T_l). \quad (8)$$

As observed from the above set of differential equations, the difference between the e-2TM and 3TM model is the consideration of the e-ph scattering process among the non-thermal hot electrons, which was ignored in e-2TM.

The coefficients a_{e-e} and b_{e-ph} represent how the non-thermal hot electrons lose energy by e-e scattering and e-ph scattering, respectively, and their values can be calculated from the e-e scattering rate τ_{e-e}^{-1} ¹⁰⁰ and the e-ph scattering rate τ_{e-ph}^{-1} ¹⁰¹ respectively. For ultrafast timescales, the lattice heat capacity C_l is a constant, but the electron heat capacity C_e is a function of temperature. For standard excitation conditions, C_e can be modeled as a linear function of electron temperature: $C_e = \gamma_e T_e$, where γ_e is the linear carrier heat capacity constant.¹⁰² All these coefficients can be obtained either from *ab initio* calculations or from phenomenologically fitting experimental data. Finally, the driving term in the above equation is the absorbed power $P_{abs}(t)$, which can be determined from the temporal profile of the optical pulse incident on the structure and the physical properties of the metallic nanostructure. One assumption of 3TM is the instantaneous decay of SPP modes, leading to the instantaneous generation of non-thermal hot electrons. This process typically occurs within ~ 10 fs,³² which is not a temporal region of interest in most cases. 3TM has been applied with a reasonable amount of success in the cases of a heavily doped semiconductor,¹⁰³ epsilon-near-zero (ENZ) materials,¹⁰⁴ and even for all-dielectric nanostructures.^{105,106} Figure 4(a) presents comparative analysis between the experimentally measured

change in the optical density ΔOD and the values calculated using the e-2TM and 3TM models.

Another model to mention in this context is quantum two-temperature model Q-2TM where the absorbed energy $P_{abs}(t)$ is divided into two parts: one used to generate thermalized hot electrons $P_{abs,th}(t)$ and the rest $P_{abs,nth}(t)$ used to generate non-thermal hot electrons. The above set of equations describing e-2TM is modified in the following manner:⁹⁶

$$\frac{dE_{nth}}{dt} = P_{abs,nth}(t) - a_{e-e}E_{nth}, \quad (9)$$

$$C_e \frac{dT_e}{dt} = a_{e-e}E_{nth} + P_{abs,th}(t) - G(T_e - T_l), \quad (10)$$

$$C_l \frac{dT_l}{dt} = G(T_e - T_l) - C_l \frac{T_l - T_0}{\tau_{\text{heat transfer}}}. \quad (11)$$

The absorption of power responsible for the creation of low-energy thermalized electrons is given by a classical expression based on the imaginary part of the dielectric permittivity according to the Drude model,⁴

$$P_{abs,th} = \text{Im}\{\epsilon_{\text{Drude}}\} \int_V dV \mathbf{E}_\omega \cdot \mathbf{E}_\omega^*. \quad (12)$$

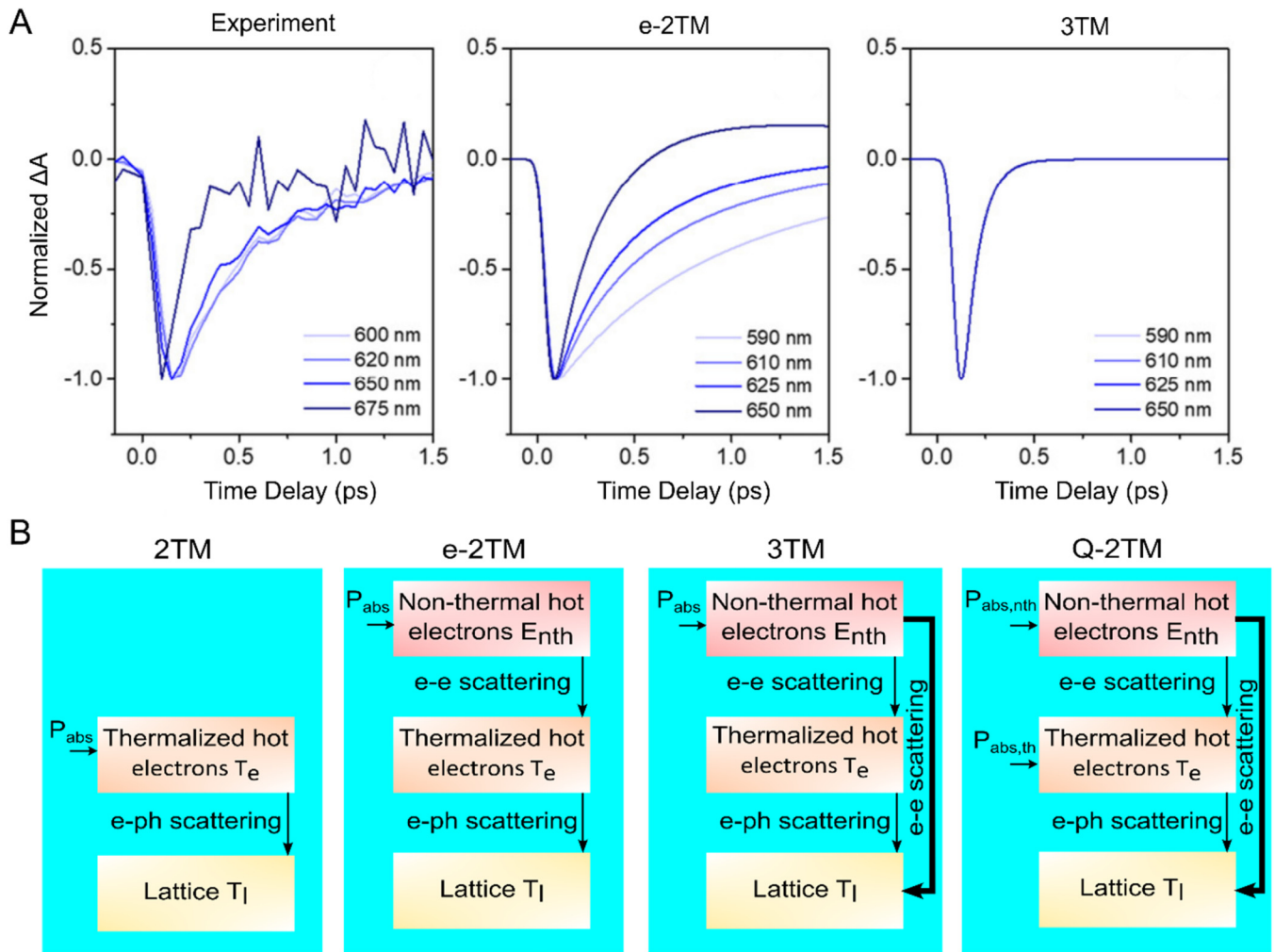
On the other hand, the generation of non-thermal hot electrons is a result of relaxed conservation of momentum at the surface of a nanostructure, and the corresponding absorbed power is derived from quantum formalism.¹⁰⁷ The quantum term $P_{abs,nth}$ becomes significant for nanostructures with smaller dimensions,⁴

$$P_{abs,nth} \approx \frac{1}{4\pi^2} \times \frac{e^2 E_F^2}{\hbar} \frac{1}{(\hbar\omega)^2} \int_S |E_{\omega,\text{normal}}|^2 dS, \quad (13)$$

where $E_{\omega,\text{normal}}$ is the projection of the electric field onto the normal to the surface, as defined above, and it is taken at points inside the nanoparticle and immediately adjacent to the surface. Figure 4(b) summarizes the key parameters considered in these temperature models and highlights the differences.

G. Dependence of optical properties on different parameters

The primary objective of the theoretical models is to anticipate alterations in observable optical characteristics so that a one-on-one comparison with the experimental data can be made. Once a system is represented in terms of the mentioned parameters of temperature models—the population of non-thermal electrons $N_{nth}(t)$, the temperature of thermalized electrons $T_e(t)$, and the lattice temperature $T_l(t)$, a relation needs to be established to make a physical connection between this set of parameters and the dielectric permittivity of the material. Modulation of the permittivity exhibits the temporal signature of hot-electron dynamics. The dynamic behavior of $N_{nth}(t)$ and $T_e(t)$ induces a transient variation in the energy distribution of electrons, denoted by $\Delta f(E, t)$. Such a variation results in an increase in the occupation probability of



10 October 2024 21:53:43

FIG. 4. Temperature models for describing hot-electron evolution. (a) Temporal cuts at different probe wavelengths of the non-thermal contribution extracted from the experimental transient absorption map and from the simulated transient absorption maps obtained by e-2TM and 3TM models. The system under consideration was 2D Au NP arrays.¹⁰⁸ (b) Comparison between different temperature models based on Refs. 4 and 7. Figure panel (a) is reproduced with permission from O’Keeffe *et al.*, Laser Photonics Rev. 15, 2100017 (2021). Copyright 2021 Wiley-VCH Verlag GmbH.

electronic states below the Fermi level and an increase in those above the Fermi level. Consequently, there is increased energy absorption through interband transitions between energy bands positioned below and above the Fermi levels. This change in absorption is represented by the change in the complex part of the metal permittivity, $\Delta\epsilon''$.¹⁰⁹ The modulation of the occupancy distribution for non-thermal carriers can be expressed as follows:⁹⁷

$$\Delta f_{nth}(E, t) = \delta_{nth}(E)N_{nth}(t), \quad (14)$$

where $\delta_{nth}(E)$ is a double-step like function,⁹⁷ which extends from $-hv$ to $+hv$ (here, hv is the energy of the excitation photon) around E_F , broadened by temperature and pump pulses¹¹⁰ and

formally given by

$$\delta_{nth}(E) = \frac{1}{A} \{ f(E - hv, T_{env})[1 - f(E, T_{env})] - f(E, T_{env})[1 - f(E + hv, T_{env})] \}. \quad (15)$$

Here, A is a constant derived from the law of conservation of energy⁹⁵ and T_{env} is the temperature of the surrounding environment. The spectral shape of Δf_{nth} is determined by the functional form of δ_{nth} , but its temporal profile is precisely the same as $E_{nth}(t)$. This assumes that all the non-thermalized hot carriers undergo relaxation at the same time-constant, and this time constant is independent of their energy.

For thermalized electrons, the disparity in the energy occupancy distribution is calculated from the difference between the excited and equilibrium Fermi–Dirac distribution,⁹⁷

$$\Delta f_{T_e}(E, t) = f(E, T_e(t)) - f(E, T_{env}). \quad (16)$$

An increased electronic temperature results in an increase in absorption due to interband transitions in a metal. This results from increased transitions toward final states below the Fermi level. This phenomenon is commonly referred to as Fermi smearing, as the electronic occupation probability becomes smeared around E_F for an increase in T_e .

The change $f(E)$ due to the non-thermal ($\Delta f_{nth}(E, t)$) and thermalized ($\Delta f(E, T_e(t))$) hot electrons should be related to the corresponding change in the complex permittivity. This can be modeled using a semiclassical model of thermos-modulation nonlinearities¹¹¹ using joint density of states (JDOS) calculations. Once the joint density of states $J_{N(T_e)}(\lambda, t)$ is calculated for the probe wavelength λ , the modulation of the imaginary part of the interband permittivity can be calculated as follows:¹¹¹

$$\Delta \epsilon''_{N(T_e)}(\lambda, t) = \frac{e^2 \lambda^2}{12\pi \epsilon_0 m^2 c^2} |p_L|^2 \Delta J_{N(T_e)}(\lambda, t). \quad (17)$$

Here, m is the free electron mass, e is the free electron charge, c is the speed of light in vacuum, and p_L is the electric-dipole matrix element of the considered transition. A detailed discussion on this calculation can be found in Ref. 111. From the imaginary part of the dielectric permittivity, the real part of the dielectric permittivity can be calculated using Kramers–Kronig relations.

Again, the change in the plasma frequency due to a change in the lattice temperature can be found using the following relation:¹¹²

$$\Delta \omega_p(t) = -\frac{1}{2} \alpha_V \omega_p \Delta T_l(t). \quad (18)$$

This leads to a corresponding variation in intraband permittivity, which can be calculated as follows:

$$\Delta \epsilon_{\omega_p}(\omega, t) = -\frac{\Delta \omega_p(t) [\Delta \omega_p(t) + 2\omega_p]}{\omega(\omega + i\Gamma)}. \quad (19)$$

To eventually determine the total photoinduced modulation of the metal permittivity, both the intraband and interband contributions to the change in permittivity are summed up, giving a complex-valued change in the dielectric permittivity. The differential optical density spectra $\Delta OD(\lambda, t)$ can be determined by iterating the calculation of the absorption of the nanostructure incrementally, considering the time-dependent modification of the optical properties of the plasmonic nanomaterial, as described by the permittivity function $\epsilon(\lambda, t) = \epsilon_0(\lambda) + \Delta \epsilon(\lambda, t)$, where $\epsilon_0(\lambda)$ is the permittivity in the absence of hot-electron excitation. The values, thus, obtained can be readily compared with the transient value of $\Delta OD(\lambda, t)$ obtained from standard transient absorption spectroscopy.

III. INVESTIGATING ULTRAFAST DYNAMICS OF HOT ELECTRONS IN PLASMONIC SYSTEMS

Though the temperature models help us represent the dynamic processes hot electrons go through in terms of a few parameters, full validation of these models necessitates experimental measurements to support the predicted behaviors as well as to quantify the free parameters. Currently, two techniques are frequently used to investigate hot-electron dynamics: photocurrent measurement and time-resolved transient absorption spectroscopy. Despite their popularity, both techniques suffer from a few limitations, thus highlighting the quest for the development of alternative characterization methods to either validate or add to the information obtained through existing approaches. In this section, we will provide a concise overview of the already well-established characterization techniques for studying ultrafast hot-electron dynamics, followed by a discussion on novel optical phenomena that can augment our current comprehension.

A. Photocurrent measurement

One of the most popular configurations in the study of hot-electron physics involves the generation of hot electrons in metallic nanostructures, followed by their collection into an adjacent semiconductor material. A Schottky barrier forms at the interface between the metal and the semiconductor, exhibiting diode-like current–voltage characteristics. Energetic hot carriers capable of overcoming this Schottky barrier can modulate the current through the Schottky diode, thus indicating the generation of hot carriers. Photocurrent measurements serve to track the efficiency of hot-carrier generation,¹¹³ distinguish between plasmon-induced and photoexcited carriers,¹¹ design efficient plasmonic photodetectors,¹⁸ and compare hot-carrier generation efficiency among different material systems.¹¹⁴ Furthermore, the wavelength and polarization dependence of photocurrent can offer interesting insights into the injection of hot carriers into 2D materials.^{115,116} However, detailed temporal profiling of the hot-carrier population cannot be resolved using photocurrent measurements alone, as it requires a detection system with temporal resolution on the order of hundreds of femtoseconds, currently beyond the capability of photocurrent measurements.

B. Transient absorption spectroscopy

The ultrafast dynamics of hot carriers can be effectively probed through time-resolved transient absorption spectroscopy, employing a pump–probe technique featuring a femtosecond pulsed laser. In this method, two synchronized laser pulses with a pulse duration shorter than the characteristic lifetime of hot electrons are required, with a controlled delay between the instants they hit the sample. A strong pump beam is used to induce a non-equilibrium state in the sample, while a relatively weaker probe beam is utilized for monitoring the pump-induced alterations in the optical properties (e.g., reflectance or transmittance) of the sample. Usually, they come from the same laser and are split using a beam splitter. The probe beam usually comprises a broadband light wave generated by a supercontinuum crystal excited by a fraction of the pump beam. The wavelength of the pump beam is

typically the same as that of the main laser. However, an optical parametric amplifier may be employed to generate a wavelength-selectable pump beam. In a standard pump-probe spectroscopy measurement, the interaction between the probe beam and the sample is recorded both in the presence and in the absence of the pump beam. Careful analysis of these measurement data reveals the modulation induced by the pump. In a time-resolved transient absorption spectroscopy system, a delay mechanism between the arrival of the pump and probe pulses allows for tracking the time-dependent transient behavior. Due to the pump beam being strong in most practical cases of interest, precautions are taken to ensure that the detection system exclusively collects the probe beam upon its interaction with the sample. This can be accomplished by spatially or spectrally filtering the pump beam. The calculation of the change in the optical density differs based on the mode of the optical characterization. In the case of a transmission-mode measurement, where the transmittance of the sample is measured before and after the incidence of the pump, the change in the optical density can be calculated using the following expression:¹¹⁷

$$\begin{aligned}\Delta OD &= OD_{\text{after pump}} - OD_{\text{before pump}}, \\ \Delta OD &= \log_{10}(T_{\text{before pump}}) - \log_{10}(T_{\text{after pump}}), \\ \Delta OD &= \log_{10}\left(\frac{T_{\text{before pump}}}{T_{\text{after pump}}}\right).\end{aligned}\quad (20)$$

Now, in the case of a reflection-mode measurement, where the change in the reflectance of the sample is recorded before and after the incidence of the pump, the optical change in the optical density is calculated using the reflectance as follows:¹¹⁸

$$\begin{aligned}\Delta OD &= OD_{\text{after pump}} - OD_{\text{before pump}}, \\ \Delta OD &= \log_{10}(R_{\text{before pump}}) - \log_{10}(R_{\text{after pump}}), \\ \Delta OD &= \log_{10}\left(\frac{R_{\text{before pump}}}{R_{\text{after pump}}}\right).\end{aligned}\quad (21)$$

In transient absorption spectroscopy, the time delay between the arrival of the pump and the probe light at the location of the sample is varied with the help of a delay line. The so-called time zero is set based on the temporal overlap between the pump and the probe light. However, for broadband probe light, a “chirp correction” needs to be performed on the raw data. The purpose is to remove the artifacts resulting from the wavelength dependence of the index of refraction of the optical elements present in the optical setup. The different frequency components of the probe light experience different amounts of time delay, and thus, the time zero for each of the wavelengths is different. It can be accomplished with the help of a prism compressor that attributes different time delays to different wavelength components of the white light probe. However, this can be done with reasonable accuracy using computational techniques.

A standard computational procedure to perform chirp correction involves finding the time zero for a few of the wavelengths, which are well separated and cover the wavelength range of interest, followed by using a fitting function for the rest of the wavelengths.

One such fitting function is

$$t_0 = a\sqrt{\frac{b\lambda^2 - 1}{c\lambda^2 - 1}} + d. \quad (22)$$

Here, there are four parameters: a, b, c, and d to be determined for the fit, λ is the wavelength of interest, and t_0 is the time zero for the wavelength λ . To determine the fitting parameters for the above function, the time zeros corresponding to four different wavelengths need to be known. While transient absorption spectroscopy remains the predominant technique for investigating hot-electron dynamics, it encounters limitations primarily stemming from measurement artifacts.^{119,120} Recently, numerous novel optical phenomena have emerged because of hot-electron generation, injection, or their interplay. These innovative optical effects serve as effective tools for corroborating and augmenting the insights gleaned from transient absorption spectroscopy.

C. Novel optical phenomena to study hot-electron dynamics

A plethora of novel optical phenomena facilitates the study of hot-electron dynamics, including ultrafast all-optical modulation of light intensity, phase, and polarization.^{118,121,122} Additionally, intriguing optical effects can be observed through transient symmetry-breaking approaches, where deliberate design of the spatial profile of generated hot electrons and their subsequent injection disrupts symmetry in the nanostructure and the electron-accepting material, respectively. This leads to the rapid generation of ultrafast linear or circular dichroism and second order-nonlinearity.^{117,123,124} Recent publications also explore the utilization of terahertz radiation,¹²⁵ a consequence of the ultra-short current burst resulting from hot-electron injection, as another effective tool for studying hot-electron dynamics.

Investigating changes in optical properties arising from hot-electron generation within metallic structures and their subsequent injection into electron-accepting materials yields valuable insights into the spatial dynamics of these energetic electrons. This leads to sub-picosecond all-optical modulation, where control light excites the LSP mode leading to the generation of hot electrons, and the transient response of the material is observed using a probe beam. Such modulation, driven by hot-electron dynamics, offers the high temporal resolution required to study the relaxation dynamics of hot electrons.

The injection of plasmonic hot electrons into a phase-change material, such as VO₂ [Fig. 5(a)], presents an effective strategy for all-optical modulation.¹²⁶ This approach is particularly advantageous due to the significant change in permittivity observed across its first-order metal-semiconductor phase transition. Achieving modulation speeds in the range of ~500 fs is feasible [Fig. 5(b)] in this configuration, and this was verified under different pump fluences [Fig. 5(c)]. Additionally, careful analysis of the transient absorption response for different polarizations unveils the non-uniformity in hot-electron injection. Moreover, different relaxation timescales serve as indicators of various carrier-dynamic processes. Therefore, accessing different temporal regimes will be crucial to unraveling carrier dynamics, which can also be leveraged for

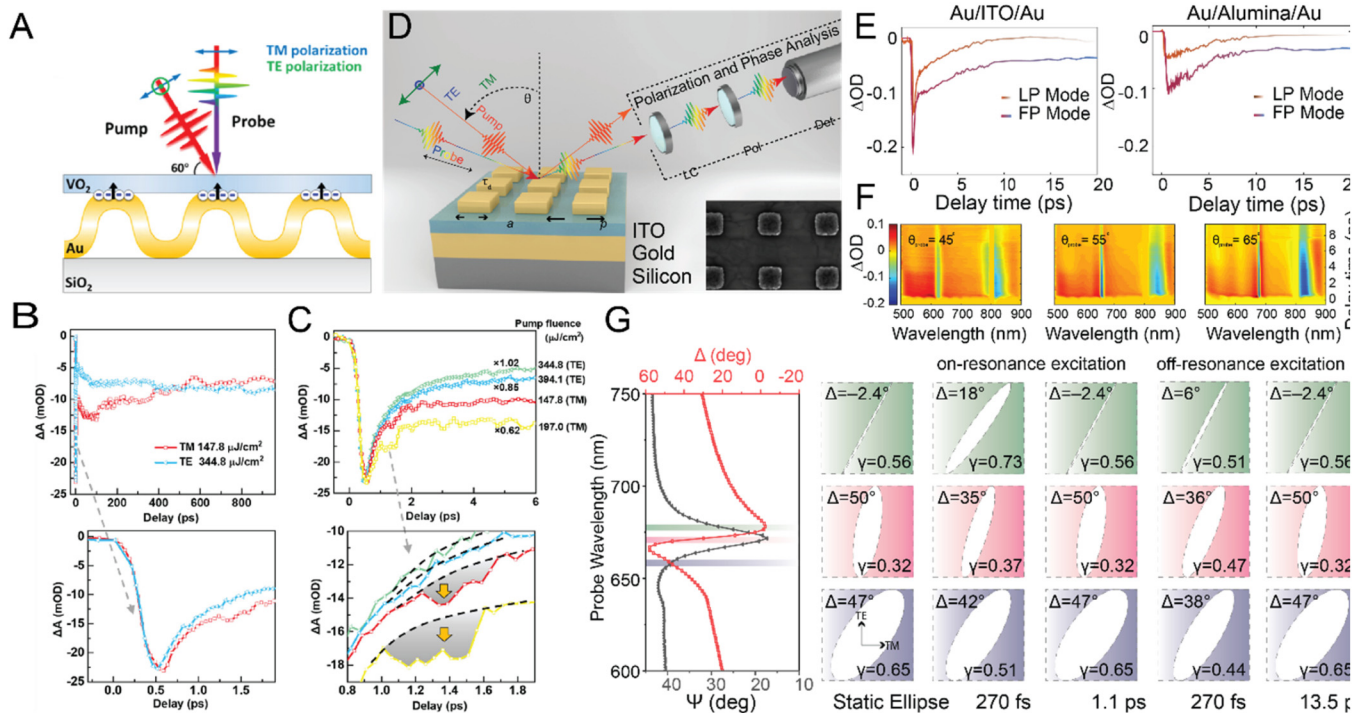


FIG. 5. All-optical modulation for studying hot-electron dynamics. (a) Schematic illustration of a self-supported VO_2 film and a gold nanoshell grating composite structure in a pump-probe setup with hot-electron injection marked by the black arrows.¹²⁶ (b) Transient absorption dynamic monitored with TM and TE polarized beams having threshold fluences. The lower panel shows the dynamics within the first 2 ps.¹²⁶ (c) Transient absorption dynamics within the first 6 ps pumped with TM-polarized and TE-polarized beams under different pump fluences. The lower panel shows the dynamics within the first 2 ps with the gray areas highlighting the effect of non-uniform hot-electron injection under TM polarization.¹²⁶ (d) Schematic of the plasmonic structure made of Au cubes on ITO along with a polarization analysis setup. Inset: SEM image of the plasmonic structure.¹²² (e) The improvement in the modulation speed in the presence of an electron-accepting material (ITO).¹¹⁸ (f) The LP mode can be modulated by changing the incident angle, but the FP mode is not sensitive to changes in the incident angle.¹¹⁸ (g) Static Ψ - Δ spectra measured at $\theta = 60^\circ$ (leftmost). The large spectral sensitivity of Δ at the vicinity of λ_{pic} originates from the narrow linewidth of the planar plasmonic crystal (PIC) mode. Static (i.e., zero delay time) polarization ellipses (second from the left) measured at the wavelengths marked by the color bars shown in the left panel. Measured polarization ellipses at delay times 270 fs and 1.1 ps following the on-resonance excitation of the plasmonic crystal (middle two panels). Measured polarization ellipses monitored at delay times 270 fs and 13.5 ps upon the off-resonance interband pumping (right two panels). The ultrafast modulation speed in the middle panel is induced by the injection of hot electrons from the gold nanoparticles into the ITO electron acceptor.¹²² Figure panels (a)–(c) are reproduced with permission from Fu *et al.*, ACS Photonics 9, 3950 (2022). Copyright 2022 American Chemical Society. Figure panels (d) and (g) are reproduced with permission from Taghinejad *et al.*, Nano Lett. 18, 5544 (2018). Copyright 2018 American Chemical Society. Figure panels (e) and (f) are reproduced with permission from Taghinejad *et al.*, Adv. Mater. 30, 1704915 (2018). Copyright 2018 Wiley-VCH Verlag GmbH.

engineering purposes, such as accelerating modulation speeds. The relaxation of hot electrons in metallic structures is dominated by electron-phonon interactions taking place on a picosecond timescale. However, the injection of hot electrons into electron-accepting materials creates another relaxation pathway for hot electrons by electron-electron interaction. The relaxation of hot electrons by electron-electron interaction is much faster and occurs on a timescale of ~ 200 fs.¹¹⁸ The onset of a new relaxation pathway allows us to study hot-electron dynamics by analyzing the ultrafast Kerr-type optical nonlinearity,^{127–129} which is a product of the modification of the temperature and the density of free carriers in metallic structures. For example, an electron-dominated relaxation channel can be introduced by extracting the hot electrons during the ultrafast time window of electron-electron scattering. The proposed structure consists of an array of Au nanocubes, which functions as a plasmonic

structure atop an ITO layer that serves as an electron-accepting material [Fig. 5(d)].¹¹⁸ The structure shows two resonance modes: (i) an angle-dependent lattice plasmon (LP) mode and (ii) an angle-independent Fabry-Perot (FP) mode. The introduction of a new relaxation pathway has resulted in a significant reduction in relaxation time across both resonance modes, as evidenced by the comparative analysis with a control sample [Fig. 5(e)]. The spectral position of the LP mode, and, consequently, the relaxation time of hot electrons, is sensitive to the angle of incidence. This sensitivity stems from the out-of-plane dipolar nature of the mode. This offers the flexibility to tune the excitation wavelength to the proper wavelength of interest by adjusting the illumination configuration. In contrast, the spectral position, and, thus, the relaxation time, of the FP mode remains unaffected by the angle of incidence [Fig. 5(f)]. Apart from the intensity, the polarization can also be modulated in an ultrafast all-optical manner as was

shown for the same configuration of Au nanocubes on the ITO layer [Fig. 5(g)].

In addition to facilitating an ultrafast relaxation channel, electron-accepting materials can serve as hosts for the injected hot electrons, triggering rapid modulations in their optical characteristics, typically occurring within a timescale of hundred femtoseconds. This effect can be utilized, for instance, to induce transient asymmetry in an otherwise centrosymmetric medium, leading to the transient generation and modulation of second harmonic optical signals within such media. Centrosymmetric media, media that possess a center of inversion symmetry, show a vanishing $\chi^{(2)}$ response according to electric-dipole approximation.^{130–132}

Generation of a second harmonic signal in such a medium requires the breaking of inversion symmetry. The inversion symmetry can be broken by the application of an external electric field utilizing the existing third order susceptibility $\chi^{(3)}(2\omega, \omega, \omega, 0)$, leading to the so-called electric-field-induced second harmonic generation (EFISH).^{133–135} Another demonstration of the breaking of inversion symmetry leading to the generation of a second harmonic signal was achieved in transition metal dichalcogenides (TMDCs) by injecting charges, named as charge-induced second harmonic generation (CHISHG).¹³⁶ The generation of hot electrons, followed by their injection into an electron-accepting material, can provide a combination of the aforementioned effects, ultimately leading to

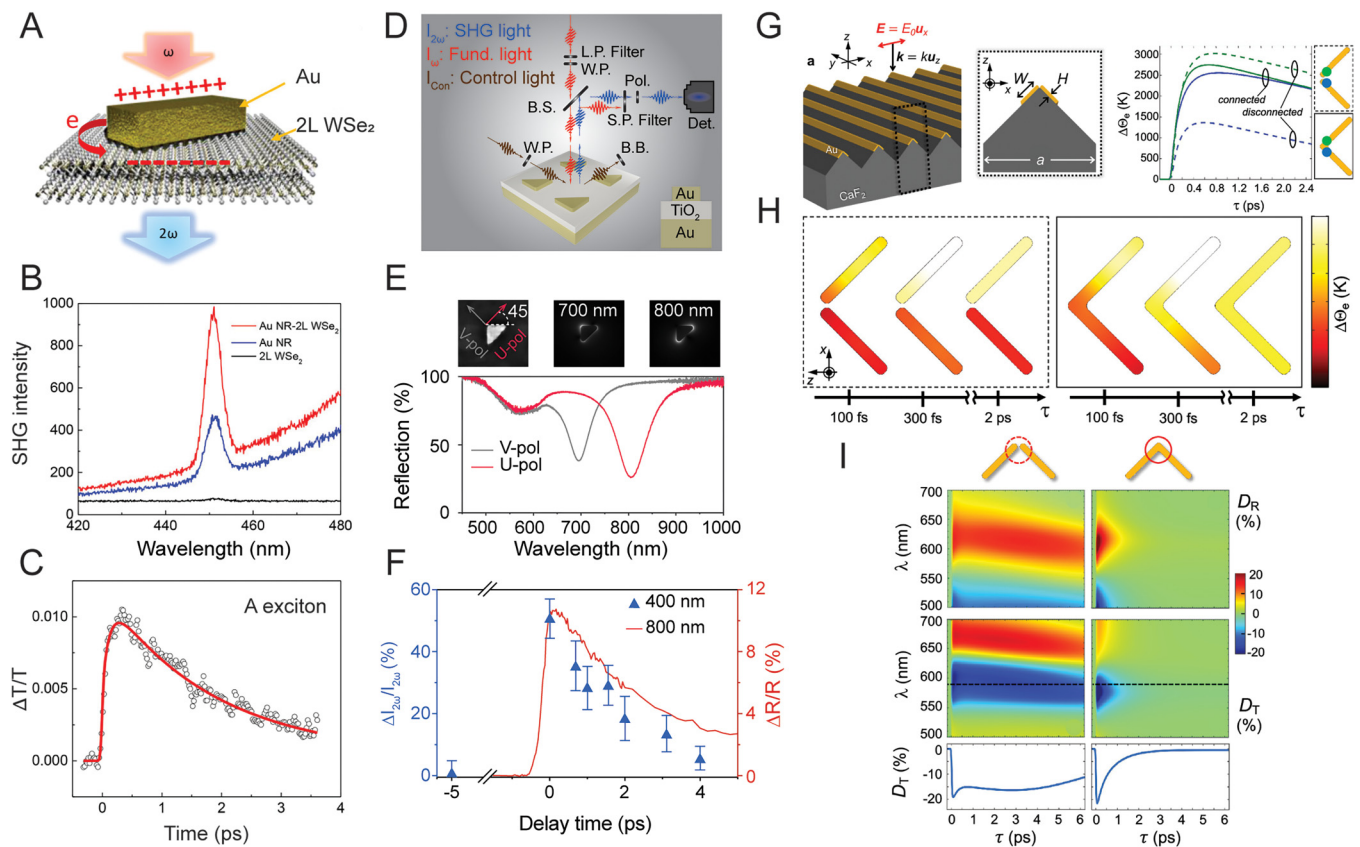


FIG. 6. Optical phenomena resulting from transient symmetry breaking induced by hot electrons. (a) Transient SHG induced by symmetry breaking using hot-carrier injection. A plasmonic structure made of Au nanorods (NR) on the top of bilayer WSe₂.¹³⁷ (b) The injection of hot carriers from the Au NRs into the bilayer WSe₂ momentarily breaks the inversion symmetry giving rise to an enhanced SHG.¹³⁷ (c) The decay kinetics of an A exciton with biexponential fitting confirming the ultrafast nature of hot-carrier injection.¹³⁷ (d) Schematic representing a plasmonic structure made of triangular Au unit cells with a simplified setup for measurement and a cross section in the inset.¹²⁴ (e) Static reflection spectra of for the two eigen polarizations and the spatial profile of the field enhancement.¹²⁴ (f) Temporal response of the normalized $\Delta I_{2\omega}$ and the transient reflection change ΔR upon the illumination of the structure with a V-polarized 700 nm control beam.¹²⁴ (g) Schematic of a plasmonic metagrating design with the unit cell in the inset (left). Temporal dynamics of hot carriers' temperature variation at two exemplary points marked in the inset (right).¹³⁶ (h) Spatial distribution of an increase in the electronic temperature T_e in the disconnected (left) and connected (right) nanostrip.¹³⁶ (i) Ultrafast symmetry recovery driven by electronic diffusion for disconnected (left) and connected (right) structures shown in terms of imbalance in the reflection diffraction order (D_R) and the transmission diffraction order (D_T).¹³⁸ Figure panels (a)–(c) are reproduced with permission from Wen *et al.*, *Nano Lett.* **18**, 1686 (2018). Copyright 2018 American Chemical Society. Figure panels (d)–(f) are reproduced with permission from Taghinejad *et al.*, *Phys. Rev. Lett.* **124**, 013901 (2020). Copyright 2020 American Physical Society. Figure panels (g)–(i) are reproduced with permission from Schirato *et al.*, *Nano Lett.* **21**, 1345 (2021). Copyright 2021 American Chemical Society.

10 October 2024 21:53:43

second harmonic generation (SHG) and modulation of the SHG signal. The interfacial Coulomb force resulting from the electric field acts on the injected electrons to bring them back to the interface, where they recombine, effectively suppressing the $\chi^{(2)}$ response within an ultrafast timescale.

Transient symmetry breaking of an otherwise centrosymmetric medium can be achieved in centrosymmetric media consisting of bilayer transition metal dichalcogenides (TMDCs), such as WSe₂.¹³⁷ A plasmonic structure, such as a periodic arrangement of Au nanorods [Fig. 6(a)], fabricated on top of a bilayer WSe₂, can be used as a source of hot electrons that are going to be injected into the WSe₂ layer. Though odd numbered TMDC layers show strong intrinsic SHG, bilayer TMDCs do not show such a response due to their centrosymmetric structure. The injection of plasmonic hot electrons into such layers momentarily breaks the symmetry resulting in strong SHG [Fig. 6(b)]. The pump laser beam cannot excite carriers in WSe₂ directly, but it can excite hot carriers in the metal disk through surface plasmon resonance. A fraction of these hot carriers are then injected into bilayer WSe₂ and occupy the conduction band of WSe₂. The injected hot carriers demonstrate a reduced probability of an electron transition from the valence band to the conduction band, resulting in the A-exciton bleaching effect, which exhibits an ultrafast temporal signature [Fig. 6(c)]. Transient symmetry breaking of a centrosymmetric medium, such as TiO₂, can also enable an increase in SHG.¹²⁴ One such demonstration involves an array of triangular Au nanostructures deposited on top of TiO₂ [Fig. 6(d)]. The structure is judiciously engineered such that two resonance modes at two different wavelengths can be accessed through two perpendicular polarizations: one giving a centrosymmetric while the other giving a non-centrosymmetric spatial

profile of the electric field [Fig. 6(e)]. The generation of hot electrons closely follows the spatial profile of the electric field enhancement.^{6,42} Thus, the creation of an asymmetric electric field profile leads to asymmetry in the locations of hot-electron generation followed by their asymmetric injection. This results in the transient breaking of centrosymmetry in the electron-accepting material, with the timescale being dominated by the retraction process of ejected hot electrons back to the plasmonic material. Analyzing the modulation in the second harmonic signal $\Delta I_{2\omega}$ [Fig. 6(f)] can provide us with important insights into the transport, injection, and lifetime of hot electrons. Another interesting demonstration of transient symmetry breaking is the ultrafast modulation in a diffraction order from metagrating achieved in Ref. 138 [Fig. 6(g)]. The most interesting finding in this study is the inhomogeneous ultrafast hot-electron dynamics [Fig. 6(h)] in both the connected and disconnected nanostrip structures that leads to sub-picosecond modulation of the reflection and transmission diffraction orders [Fig. 6(i)].

Another important optical effect emerging from transient symmetry breaking is the ultrafast control over the polarization of light. Hot electron-induced changes in the electronic temperature can be utilized to create spatiotemporal asymmetry in a rationally designed structure, as demonstrated using a triangle-on-grating structure and a nanocross structure.^{117,123} For the triangle-on-grating structure, numerical simulations reveal spatial maps of the electron temperature T_e at different time snapshots [Fig. 7(a)], which demonstrate the pump polarization-induced symmetry breaking, as evidenced by the distinct differences observed at the two termini [Fig. 7(b)]. Once the structure is probed with circularly polarized light, it exhibits a handedness-selective response in a

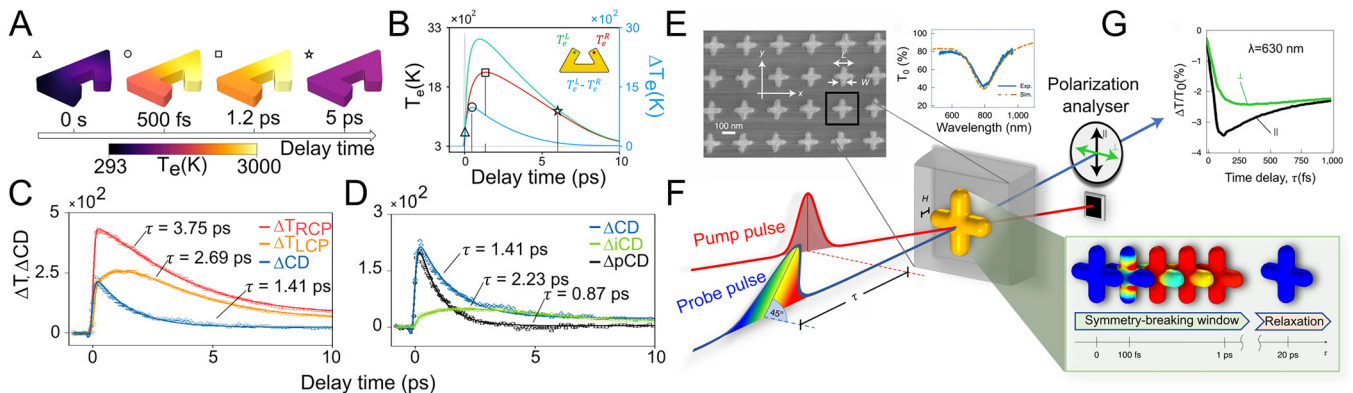


FIG. 7. Ultrafast transient dichroism mediated by hot-electron dynamics. (a) Numerically calculated spatial maps of the electron temperature T_e at different timestamps.¹¹⁷ (b) Temporal evolution of T_e at the two terminuses and their differences.¹¹⁷ (c) Transient curves and the decay time constants of ΔT_{LCP} , ΔT_{RCP} , and the ΔCD response observed at $\lambda = 684$ nm under $+50^\circ$ pump excitation.¹¹⁷ (d) The ΔCD curve is then decomposed to temporal profiles of ΔiCD and ΔpCD , where the decay timescales provide insights into the primary contributing factor among different hot-electron-related mechanisms for each feature.¹¹⁷ (e) SEM image of nanocrosses (left) and measured (blue) and simulated (orange) transmittance of the polarization-insensitive unperturbed structure (right).¹²³ (f) Sketch of the polarization-resolved pump-probe setup utilized to experimentally reveal the ultrafast optical dichroism (left). Cartoon of the transient permittivity pattern (evaluated at around 630 nm) evolving over time at the nanoscale (right).¹²³ (g) Experimentally obtained differential transmission signal at 630 nm after photoexcitation when the probe polarization is parallel (black) or perpendicular (green) to the pump field.¹²³ Figure panels (a)–(d) are reproduced with permission from Kim *et al.*, Proc. Natl. Acad. Sci. U.S.A. **121**, 13 (2024). Copyright 2024 Author(s), licensed under a Creative Commons Attribution-Non-Commercial-No Derivatives License 4.0 (CC BY-NC-ND). Figure panels (e)–(g) are reproduced with permission from Schirato *et al.*, Nat. Photonics **14**, 723 (2020). Copyright 2020 Springer Nature Limited.

transient manner. This is demonstrated by the differential transmittance of the left and right circularly polarized light components upon excitation by the pump [Fig. 7(c)]. Though the geometric structure of the system inherently exhibits a degree of intrinsic

chirality, the pump-induced chirality is the dominant contributor, as the pump-induced circular dichroism ΔpCD significantly outweighs the inherent circular dichroism ΔiCD response at early timescales [Fig. 7(d)]. The restoration of the mirror symmetry of

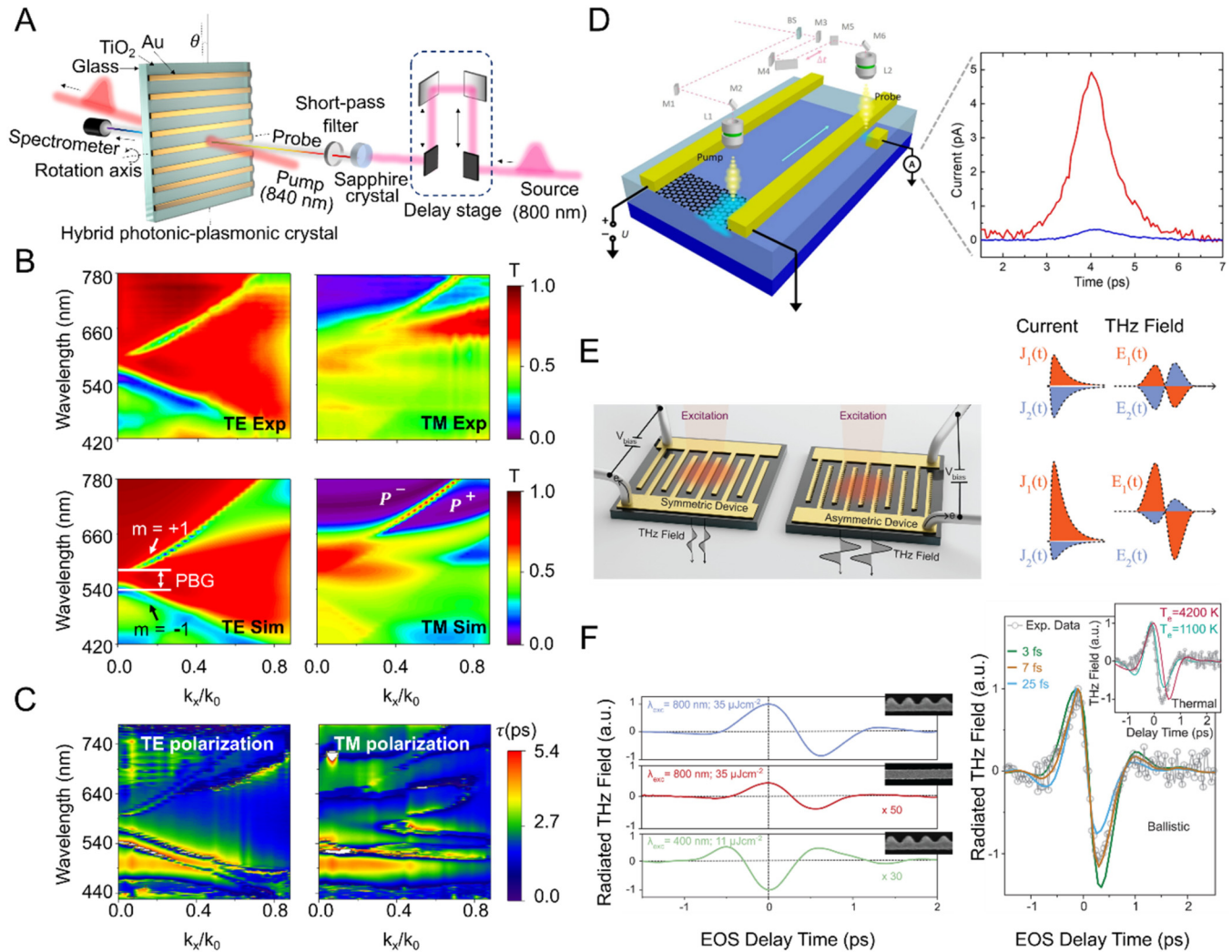


FIG. 8. THz emission for determining hot-carrier transport dynamics and tunable dispersion in recovery speeds. (a) Schematic of an angle-resolved transient pump-probe spectroscopy setup. Both the pump and the probe pulses are generated from a pulsed laser with a center wavelength of 800 nm. An optical parametric amplifier is used to generate a narrowband pump pulse with a center wavelength of 840 nm. Broadband probe pulses are generated through supercontinuum generation using a nonlinear crystal.¹⁴¹ (b) Angular dispersion for optical transmission for a hybrid photonic-plasmonic crystal under TE and TM polarization in experiment (top) and simulation (bottom).¹⁴¹ (c) Angular dispersion of recovery time constants for TE and TM polarization.¹⁴¹ (d) The on-chip pump-probe measurement setup. The field is coupled with an Auston switch (detector) using a transmission (left). A strongly enhanced THz field observed from the hybrid device (red) over the graphene-free device (navy) (right).¹⁴⁷ (e) Schematic of two arrays (one symmetric and the other asymmetric) of electrically enabled plasmonic antennas for studying the spatiotemporal transport dynamics of hot-electron transport through THz radiation (left). The interfacial transport of hot carriers generates two counterpropagating current pulses and their corresponding THz bursts. The THz field is canceled in the case of the symmetric device, but the asymmetric device gives rise to non-zero far-field THz emission (right).¹²⁵ (f) Temporal waveforms of the recorded THz electric fields under different conditions with the SEM images in the inset (left). A comparison between the temporal profile of the measured THz field (data points) and modeled waveforms (solid line) for three temporal regimes of ballistic transport. Inset: measured THz field (data points) and modeled waveforms (solid line) considering only thermal contribution (right).¹²⁵ Figure panels (a)–(c) are reproduced with permission from Kim *et al.*, *Adv. Sci.* **10**, 2205434 (2023). Copyright 2023 Author(s), licensed under a Creative Commons Attribution (CC BY) license. Figure panel (d) is reproduced with permission from Zhang *et al.*, *Nat. Commun.* **13**, 6404 (2022). Copyright 2022 Author(s), licensed under a Creative Commons Attribution 4.0 International License. Figure panels (e) and (f) are reproduced with permission from Taghinejad *et al.*, *Science* **382**, 299 (2023). Copyright 2023 The American Association for the Advancement of Science.

10 October 2024 21:53:43

the refractive index is dictated by the spatial diffusion of the electron temperature over time.^{139,140} This is a relatively recent technique for obtaining transient optical behavior at an ultrafast timescale, not limited by the comparatively slower electron–phonon interaction.^{118,141,142} The control over polarization is also visible for periodic nanocross structures [Fig. 7(e), left], which shows ultrafast transient dichroism for probe light polarized either parallel or perpendicular to the polarization of the pump light [Fig. 7(e), right]. Polarization-resolved experimental characterization [Fig. 7(f)] was conducted, with the resulting data subsequently verified using the inhomogeneous three-temperature model [Fig. 7(g)].

While transient absorption spectroscopy offers decent temporal resolution, it lacks the ability to elucidate the dynamics of hot-carrier transport across the junction between the plasmonic metal and the electron-accepting material. Conversely, monitoring the rapid changes in optical properties induced by hot-carrier injection only captures a subset of hot carriers, failing to distinguish between ballistic and thermally equilibrated carriers. Moreover, the nonlinear relationship between resonance and the change in the refractive index leads to tunable dispersion of recovery speeds, as demonstrated in Ref. 141 employing a hybrid photonic–plasmonic crystal [Fig. 8(a)]. The angular dispersions for optical transmission under both TE and TM polarization [Fig. 8(b)] are closely mimicked by the recovery speed [Fig. 8(c)], which can be tailored through the interplay among resonance modes. Consequently, there exists substantive uncertainty over recovery speed-based transient optical measurements to reliably track the lifetime of hot-carrier dynamics. A promising alternative to circumvent the interplay among resonance modes influencing the recovery speed is to measure the changes occurring exclusively due to the electrons being injected into the electron-accepting material. This can be accomplished by utilizing a probe wavelength in the mid-infrared (mid-IR) region of the spectrum.¹⁴³

Though the non-radiative decay of surface plasmons lies at the core of hot-electron physics, recent observations entail detecting and quantifying far-field terahertz (THz) emission originating from current bursts induced by hot-electron injection.¹²⁵ The injection of hot carriers from a noble metal plasmonic structure into an electron-accepting material gives rise to a momentary current pulse, with its duration constrained by the hot-carrier transport and injection time. This momentary pulse of current gives rise to electromagnetic radiation in the terahertz (THz) spectral range $\epsilon_{\text{THz}}(t)$, which is a well-known classical electrodynamic phenomenon.¹⁴⁴ The idea of recording such interfacial current on a femto-second timescale by THz emission was used in Ref. 145. Passive THz imaging was used to track hot-electron kinetics in Ref. 146. On the other hand, conventional photoconductive switches suffer from a fundamental tradeoff between an ultrafast response and output power when generating terahertz (THz) emission. This limitation can be overcome by employing a graphene-silicon hybrid photoconductive switch design that utilizes the ultrafast hot-electron injection process [Fig. 8(d)].¹⁴⁷ Finally, there has been a long-standing debate over the nature of hot-carrier injection: whether it occurs via ballistic or thermalized hot carriers.¹⁴⁸ The entire concept of carrier injection has been called into question, with attempts made to explain numerous experimental observations solely through the heating of nanoparticles.¹⁴⁹ However,

recent studies on hot-carrier transport based on terahertz (THz) emission in Ref. 125 provide significant insights that help resolve this debate. For this purpose, designer nano-antennas with broken symmetry were utilized, which led to the observed far-field THz emission [Fig. 8(e)]. Analysis of the amplitude, polarization, and temporal evolution of the THz emission can offer considerable insights into the nature (ballistic or thermalized) of the hot carriers [Fig. 8(f)]. These analyses demonstrate that the contribution of thermalized hot carriers can be safely ignored in functionalities relying on the interfacial transport of hot carriers.

IV. CONCLUSION AND OUTLOOK

The inevitable loss in plasmonics initially hindered its widespread adoption in optics, notwithstanding a few notable exceptions, despite its substantial potential for miniaturizing optical devices beyond the diffraction limit.^{43,44} However, a significant turning point emerged with the thorough investigation of one such loss mechanism: the non-radiative decay of a surface plasmon polariton and localized surface plasmon modes, leading to the generation of hot carriers, thereby paving the way for the utilization of the loss.¹⁵⁰ Though the applications of hot carriers in fields, such as photocatalysis and photovoltaics, have been extensively studied, recent focus has shifted toward the ultrafast dynamics of hot carriers and exploring relevant opportunities for practical use.

Such interest is the primary motivation for this Perspective, where we approach the vast research field of active plasmonics from the viewpoint of establishing the efficacy of active plasmonic devices as a reliable platform for understanding the origination and dynamics of hot electrons. The generation of hot carriers depends strongly on the electric field strength. Enormous enhancement of the electric field can be achieved with the help of plasmonic nanostructures, and as a result, they serve the purpose of such scientific inquiry.

Recent progress in analytical and computational modeling tools has enabled the design of plasmonic nanostructures tailored for efficient hot-electron generation. Modeling the dynamics of hot electrons based on the exchange of energy through electron–electron and electron–phonon scattering has reduced the over-reliance on numerical modeling tools that lack insights into the sequence of physical processes a system undergoes and the ultrafast timescales involved in each step.

Advancements in nanofabrication techniques have facilitated the creation of innovative plasmonic structures to study ultrafast transient optical effects mediated by the generation, transport, and injection of hot carriers. Moreover, the introduction of electron-accepting materials adjacent to plasmonic nanostructures provides another control parameter to initiate and study interesting physical phenomena associated with the injection and decay of such out-of-equilibrium carriers. This approach also opens a number of choices for metal–semiconductor material combinations. Another dimension to the choice of material combination was reached with the use of two-dimensional materials, as was briefly discussed. The experimental investigation of hot-carrier lifetimes has been significantly enhanced by time-resolved pump–probe spectroscopy using femtosecond pulsed lasers, owing to the high temporal resolution and high peak power they offer. The

ability to resolve physical phenomena on a timescale of hundreds of femtoseconds allows researchers to track the rapid dynamics of hot carriers.

The transient optical response driven by electrons in plasmonic nanostructures that are temporarily out of thermal equilibrium, originally explored for an active nonlinear response and ultrafast reconfigurability, has emerged as a topic of significant importance for both fundamental research and potential future applications. Current scientific endeavors involving transient optical phenomena have provided valuable insights into the physics of hot-carrier dynamics and, thus, laid the foundation for a diverse range of applications, such as all-optical modulation, ultrafast data processing, high-speed optical switching, terahertz generation, and solar energy harvesting, to name a few. Though in its early stages, the correlation between a near-field plasmonic response and a hot-electron transport trajectory offers potential for coherent optoelectronic functionalities in small-scale devices. With more than a century of study, hot-carrier research continues to offer opportunities for exploration, fueled by both advancements in computational modeling and experimental findings.

ACKNOWLEDGMENTS

This work was supported in part by the National Science Foundation (NSF) under Grant No. DMR-2004749 and in part by the Early Stage Innovations (ESI) program of the National Aeronautics and Space Administration (NASA) under Grant No. 80NSSC23K0195 (subcontract from Baylor University; PI: Dr. Alan X. Wang).

AUTHOR DECLARATIONS

Conflict of Interest

The authors have no conflicts to disclose.

Author Contributions

Anjan Goswami: Conceptualization (equal); Investigation (lead); Writing – original draft (lead); Writing – review & editing (equal).
Andrew S. Kim: Investigation (supporting); Writing – original draft (supporting); Writing – review & editing (supporting).
Wenshan Cai: Conceptualization (equal); Funding acquisition (lead); Project administration (lead); Supervision (lead); Writing – review & editing (equal).

DATA AVAILABILITY

Data sharing is not applicable to this article as no new data were created or analyzed in this study.

REFERENCES

- ¹H. Hertz, *Ann. Phys.* **267**, 983 (1887).
- ²M. Niaz, S. Klassen, B. McMillan, and D. Metz, *Sci. Educ.* **94**, 903 (2010).
- ³L. H. Nicholls, T. Stefaniuk, M. E. Nasir, F. J. Rodríguez-Fortuño, G. A. Wurtz, and A. V. Zayats, *Nat. Commun.* **10**, 2967 (2019).
- ⁴L. V. Besteiro, P. Yu, Z. Wang, A. W. Holleitner, G. V. Hartland, G. P. Wiederrecht, and A. O. Govorov, *Nano Today* **27**, 120 (2019).
- ⁵C. Clavero, *Nat. Photonics* **8**, 95 (2014).

- ⁶M. L. Brongersma, N. J. Halas, and P. Nordlander, *Nat. Nanotechnol.* **10**, 25 (2015).
- ⁷A. Schirato, M. Maiuri, G. Cerullo, and G. Della Valle, *Nanophotonics* **12**, 1 (2023).
- ⁸B. Hou, L. Shen, H. Shi, R. Kapadia, and S. B. Cronin, *Phys. Chem. Chem. Phys.* **19**, 2877 (2017).
- ⁹Y. Kang, Y. Gong, Z. Hu, Z. Li, Z. Qiu, X. Zhu, P. M. Ajayan, and Z. Fang, *Nanoscale* **7**, 4482 (2015).
- ¹⁰C. Zhang, H. Zhao, L. Zhou, A. E. Schlather, L. Dong, M. J. McClain, D. F. Swearer, P. Nordlander, and N. J. Halas, *Nano Lett.* **16**, 6677 (2016).
- ¹¹B. Y. Zheng, H. Zhao, A. Manjavacas, M. McClain, P. Nordlander, and N. J. Halas, *Nat. Commun.* **6**, 7797 (2015).
- ¹²L. Mascaretti and A. Naldoni, *J. Appl. Phys.* **128**, 041101 (2020).
- ¹³Y. Zhang, S. He, W. Guo, Y. Hu, J. Huang, J. R. Mulcahy, and W. D. Wei, *Chem. Rev.* **118**, 2927 (2017).
- ¹⁴L. Zhou, D. F. Swearer, C. Zhang, H. Robotjazi, H. Zhao, L. Henderson, L. Dong, P. Christopher, E. A. Carter, P. Nordlander, and N. J. Halas, *Science* **362**, 69 (2018).
- ¹⁵D. J. Farrell, H. Sodabanlu, Y. Wang, M. Sugiyama, and Y. Okada, *Nat. Commun.* **6**, 8685 (2015).
- ¹⁶J. Kong, A. Rose, C. Yang, X. Wu, J. Merlo, M. Burns, M. Naughton, and K. Kempa, *Opt. Express* **23**, A1087 (2015).
- ¹⁷Z. Yuan, Z. Wu, S. Bai, Z. Xia, W. Xu, T. Song, H. Wu, L. Xu, J. Si, and Y. Jin, *Adv. Energy Mater.* **5**, 1500038 (2015).
- ¹⁸H. Chalabi, D. Schoen, and M. L. Brongersma, *Nano Lett.* **14**, 1374 (2014).
- ¹⁹D. Sil, K. D. Gilroy, A. Niaux, A. Boulesbaa, S. Neretina, and E. Borguet, *ACS Nano* **8**, 7755 (2014).
- ²⁰B. Feng, J. Zhu, B. Lu, F. Liu, L. Zhou, and Y. Chen, *ACS Nano* **13**, 8433 (2019).
- ²¹H. Tang, C.-J. Chen, Z. Huang, J. Bright, G. Meng, R.-S. Liu, and N. Wu, *J. Chem. Phys.* **152**, 220901 (2020).
- ²²S. Hüfner, *Photoelectron Spectroscopy: Principles and Applications* (Springer Science & Business Media, 2013).
- ²³Z. Fang, Y. Wang, Z. Liu, A. Schlather, P. M. Ajayan, F. H. Koppens, P. Nordlander, and N. J. Halas, *ACS Nano* **6**, 10222 (2012).
- ²⁴K. Appavoo, B. Wang, N. F. Brady, M. Seo, J. Nag, R. P. Prasankumar, D. J. Hilton, S. T. Pantelides, and R. F. Haglund, Jr., *Nano Lett.* **14**, 1127 (2014).
- ²⁵S. K. Chamoli, G. Verma, S. C. Singh, and C. Guo, *Nanoscale* **13**, 1311 (2021).
- ²⁶R. Sundararaman, P. Narang, A. S. Jermyn, W. A. Goddard III, and H. A. Atwater, *Nat. Commun.* **5**, 5788 (2014).
- ²⁷J. Khurgin, A. Y. Bykov, and A. V. Zayats, “Hot-electron dynamics in plasmonic nanostructures,” *arXiv:2302.10247* (2023).
- ²⁸W. Li and J. G. Valentine, *Nanophotonics* **6**, 177 (2017).
- ²⁹J. B. Khurgin, *Nanophotonics* **9**, 453 (2020).
- ³⁰P. Bharadwaj, B. Deutsch, and L. Novotny, *Adv. Opt. Photonics* **1**, 438 (2009).
- ³¹L. D. Landau, *Usp. Fiz. Nauk* **93**, 527 (1967).
- ³²X. Li, D. Xiao, and Z. Zhang, *New J. Phys.* **15**, 023011 (2013).
- ³³P. Nilsson, C. Norris, and L. Walldén, *Phys. Kondens. Mater.* **11**, 220 (1970).
- ³⁴W. L. Barnes, A. Dereux, and T. W. Ebbesen, *Nature* **424**, 824 (2003).
- ³⁵S. A. Maier, *Plasmonics: Fundamentals and Applications* (Springer, 2007), Vol. 1.
- ³⁶J. A. Schuller, E. S. Barnard, W. Cai, Y. C. Jun, J. S. White, and M. L. Brongersma, *Nat. Mater.* **9**, 193 (2010).
- ³⁷C. F. Bohren, *Am. J. Phys.* **51**, 323 (1983).
- ³⁸E. Altewischer, M. Van Exter, and J. Woerdman, *Nature* **418**, 304 (2002).
- ³⁹A. Akimov, A. Mukherjee, C. Yu, D. Chang, A. Zibrov, P. Hemmer, H. Park, and M. Lukin, *Nature* **450**, 402 (2007).
- ⁴⁰F. Zhou, Y. Liu, and W. Cai, *Opt. Lett.* **39**, 1302 (2014).
- ⁴¹S. Piltan and D. Sievenpiper, *J. Opt.* **20**, 055401 (2018).
- ⁴²A. O. Govorov, H. Zhang, H. V. Demir, and Y. K. Gun'ko, *Nano Today* **9**, 85 (2014).
- ⁴³M. L. Brongersma and V. M. Shalav, *Science* **328**, 440 (2010).
- ⁴⁴D. K. Gramotnev and S. I. Bozhevolnyi, *Nat. Photonics* **4**, 83 (2010).

- ⁴⁵I. Epstein, D. Alcaraz, Z. Huang, V.-V. Pusapati, J.-P. Hugonin, A. Kumar, X. M. Deputy, T. Khodkov, T. G. Rappoport, J.-Y. Hong, and N. M. R. Peres, *Science* **368**, 1219 (2020).
- ⁴⁶M. Kuttge, F. J. García de Abajo, and A. Polman, *Nano Lett.* **10**, 1537 (2010).
- ⁴⁷S. Peng, J. M. McMahon, G. C. Schatz, S. K. Gray, and Y. Sun, *Proc. Natl. Acad. Sci. U.S.A.* **107**, 14530 (2010).
- ⁴⁸O. A. Yeshchenko, I. M. Dmitruk, A. A. Alexeenko, A. V. Kotko, J. Verdall, and A. O. Pinchuk, *Plasmonics* **7**, 685 (2012).
- ⁴⁹A. Lesuffleur, H. Im, N. C. Lindquist, and S.-H. Oh, *Appl. Phys. Lett.* **90**, 243110 (2007).
- ⁵⁰Y. Nishijima, L. Rosa, and S. Juodkazis, *Opt. Express* **20**, 11466 (2012).
- ⁵¹R. H. Fowler, *Phys. Rev.* **38**, 45 (1931).
- ⁵²J. B. Khurgin, *Faraday Discuss.* **214**, 35 (2019).
- ⁵³H. Petek and S. Ogawa, *Prog. Surf. Sci.* **56**, 239 (1997).
- ⁵⁴C. Schmuttenmaer, M. Aeschlimann, J. W. Herman, R. D. Miller, D. Mantell, J. Cao, and Y. Gao, "Femtosecond studies of carrier relaxation processes at single crystal metal surfaces," *Proc. SPIE* **2125**, 98 (1994).
- ⁵⁵M. Bauer, A. Marienfeld, and M. Aeschlimann, *Prog. Surf. Sci.* **90**, 319 (2015).
- ⁵⁶T. V. Shahbazyan, *Phys. Rev. B* **94**, 235431 (2016).
- ⁵⁷A. V. Uskov, J. B. Khurgin, I. V. Smetanin, I. E. Protsenko, and N. V. Nikonorov, *J. Phys. Chem. Lett.* **13**, 997 (2022).
- ⁵⁸A. J. Leenheer, P. Narang, N. S. Lewis, and H. A. Atwater, *J. Appl. Phys.* **115**, 134301 (2014).
- ⁵⁹G. Tagliabue, A. S. Jermyn, R. Sundararaman, A. J. Welch, J. S. DuChene, R. Pala, A. R. Davoyan, P. Narang, and H. A. Atwater, *Nat. Commun.* **9**, 3394 (2018).
- ⁶⁰M. E. Sykes, J. W. Stewart, G. M. Akselrod, X.-T. Kong, Z. Wang, D. J. Gosztola, A. B. Martinson, D. Rosenmann, M. H. Mikkelsen, A. O. Govorov, and G. P. Wiederrecht, *Nat. Commun.* **8**, 986 (2017).
- ⁶¹Y. L. Wong, H. Jia, A. Jian, D. Lei, A. I. El Abed, and X. Zhang, *Nanoscale* **13**, 2792 (2021).
- ⁶²D. Hoeing, F. Schulz, N. S. Mueller, S. Reich, and H. Lange, *J. Chem. Phys.* **152**, 064710 (2020).
- ⁶³M. Hu, L. Yang, H. Dai, and S. He, *Sci. Rep.* **7**, 4809 (2017).
- ⁶⁴A. M. Brown, R. Sundararaman, P. Narang, W. A. Goddard III, and H. A. Atwater, *ACS Nano* **10**, 957 (2016).
- ⁶⁵G. Tagliabue, J. S. DuChene, M. Abdellah, A. Habib, D. J. Gosztola, Y. Hattori, W.-H. Cheng, K. Zheng, S. E. Canton, R. Sundararaman, and J. Sá, *Nat. Mater.* **19**, 1312 (2020).
- ⁶⁶Z. Lian, M. Sakamoto, H. Matsunaga, J. J. M. Vequizo, A. Yamakata, M. Haruta, H. Kurata, W. Ota, T. Sato, and T. Teranishi, *Nat. Commun.* **9**, 2314 (2018).
- ⁶⁷M. Grajower, U. Levy, and J. B. Khurgin, *ACS Photonics* **5**, 4030 (2018).
- ⁶⁸A. Manjavacas, J. G. Liu, V. Kulkarni, and P. Nordlander, *ACS Nano* **8**, 7630 (2014).
- ⁶⁹E. Y. Santiago, L. V. Besteiro, X.-T. Kong, M. A. Correa-Duarte, Z. Wang, and A. O. Govorov, *ACS Photonics* **7**, 2807 (2020).
- ⁷⁰Y. Tian, X. Shi, C. Lu, X. Wang, and S. Wang, *Electrochem. Commun.* **11**, 1603 (2009).
- ⁷¹C. Kittel and P. McEuen, *Introduction to Solid State Physics* (John Wiley & Sons, 2018).
- ⁷²G. Zhao, H. Kozuka, and T. Yoko, *Thin Solid Films* **277**, 147 (1996).
- ⁷³R. Eastment and C. Mee, *J. Phys. F: Met. Phys.* **3**, 1738 (1973).
- ⁷⁴M. G. Helander, M. Greiner, Z. Wang, W. M. Tang, and Z. Lu, *J. Vac. Sci. Technol. A* **29**, 011019 (2011).
- ⁷⁵K. Yoshida, T. Aoki, A. Suzuki, T. Matsushita, and M. Okuda, *J. Vac. Soc. Jpn.* **51**, 172 (2008).
- ⁷⁶Y. Park, V. Choong, Y. Gao, B. R. Hsieh, and C. W. Tang, *Appl. Phys. Lett.* **68**, 2699 (1996).
- ⁷⁷W. Wang, Q. Feng, K. Jiang, J. Huang, X. Zhang, W. Song, and R. Tan, *Appl. Surf. Sci.* **257**, 3884 (2011).
- ⁷⁸M. Grätzel, *Nature* **414**, 338 (2001).
- ⁷⁹S. Linic, P. Christopher, and D. B. Ingram, *Nat. Mater.* **10**, 911 (2011).
- ⁸⁰G. Magesh, B. Viswanathan, R. Viswanath, and T. Varadarajan, *Photocatalytic Behavior of CeO₂-TiO₂ System for the Degradation of Methylene Blue* (CSIR, 2009).
- ⁸¹E. Taft, H. Philipp, and L. Apker, *Phys. Rev.* **110**, 876 (1958).
- ⁸²A. O. Govorov, H. Zhang, and Y. K. Gun'ko, *J. Phys. Chem. C* **117**, 16616 (2013).
- ⁸³K. Burke, J. Werschnik, and E. Gross, *J. Chem. Phys.* **123**, 062206 (2005).
- ⁸⁴A. K. Dhara and S. K. Ghosh, *Phys. Rev. A* **35**, 442 (1987).
- ⁸⁵E. Runge and E. K. Gross, *Phys. Rev. Lett.* **52**, 997 (1984).
- ⁸⁶L. Wang, R. Long, and O. V. Prezhdo, *Annu. Rev. Phys. Chem.* **66**, 549 (2015).
- ⁸⁷J. A. Tomko, E. L. Runnerstrom, Y.-S. Wang, W. Chu, J. R. Nolen, D. H. Olson, K. P. Kelley, A. Cleri, J. Nordlander, J. D. Caldwell, and O. V. Prezhdo, *Nat. Nanotechnol.* **16**, 47 (2021).
- ⁸⁸R. Long and O. V. Prezhdo, *J. Am. Chem. Soc.* **136**, 4343 (2014).
- ⁸⁹Z. Nie, R. Long, L. Sun, C.-C. Huang, J. Zhang, Q. Xiong, D. W. Hewak, Z. Shen, O. V. Prezhdo, and Z.-H. Loh, *ACS Nano* **8**, 10931 (2014).
- ⁹⁰J. Zuloaga, E. Prodan, and P. Nordlander, *Nano Lett.* **9**, 887 (2009).
- ⁹¹R. Esteban, A. G. Borisov, P. Nordlander, and J. Aizpurua, *Nat. Commun.* **3**, 825 (2012).
- ⁹²H. Zhang and A. O. Govorov, *J. Phys. Chem. C* **118**, 7606 (2014).
- ⁹³P. Sharma, S. Tyaginov, Y. Wimmer, F. Rudolf, K. Rupp, M. Bina, H. Enichlmair, J.-M. Park, R. Minixhofer, H. Ceric, and T. Grasser, *IEEE Trans. Electron Devices* **62**, 1811 (2015).
- ⁹⁴P. B. Allen, *Phys. Rev. Lett.* **59**, 1460 (1987).
- ⁹⁵E. Carpena, *Phys. Rev. B* **74**, 024301 (2006).
- ⁹⁶P. M. Platzman and P. A. Wolff, *Waves and Interactions in Solid State Plasmas* (Academic Press, New York, 1973), Vol. 13.
- ⁹⁷C.-K. Sun, F. Vallée, L. Acioli, E. Ippen, and J. Fujimoto, *Phys. Rev. B* **50**, 15337 (1994).
- ⁹⁸A. Mazzanti, Z. Yang, M. G. Silva, N. Yang, G. Rizza, P.-E. Coulon, C. Manzoni, A. M. de Paula, G. Cerullo, G. Della Valle, and M.-P. Pileni, *Proc. Natl. Acad. Sci. U.S.A.* **116**, 8161 (2019).
- ⁹⁹M. Conforti and G. Della Valle, *Phys. Rev. B* **85**, 245423 (2012).
- ¹⁰⁰D. Pines, *Theory of Quantum Liquids: Normal Fermi Liquids* (CRC Press, 2018).
- ¹⁰¹R. H. Groeneveld, R. Sprik, and A. Lagendijk, *Phys. Rev. B* **51**, 11433 (1995).
- ¹⁰²N. W. Ashcroft and N. D. Mermin, *Solid State Physics* (Cengage Learning, 2022).
- ¹⁰³F. Scotognella, G. Della Valle, A. R. Srimath Kandada, D. Dorfs, M. Zavelani-Rossi, M. Conforti, K. Miszta, A. Comin, K. Korobchevskaya, G. Lanzani, and L. Manna, *Nano Lett.* **11**, 4711 (2011).
- ¹⁰⁴M. Z. Alam, I. De Leon, and R. W. Boyd, *Science* **352**, 795 (2016).
- ¹⁰⁵A. Mazzanti, E. A. A. Pogna, L. Ghirardini, M. Celebrano, A. Schirato, G. Marino, A. Lemaître, M. Finazzi, C. De Angelis, G. Leo, and G. Cerullo, *Small Sci.* **1**, 2000079 (2021).
- ¹⁰⁶R. Gaspari, G. Della Valle, S. Ghosh, I. Kriegel, F. Scotognella, A. Cavalli, and L. Manna, *Nano Lett.* **17**, 7691 (2017).
- ¹⁰⁷L. V. Besteiro, X.-T. Kong, Z. Wang, G. Hartland, and A. O. Govorov, *ACS Photonics* **4**, 2759 (2017).
- ¹⁰⁸P. O'Keefe, D. Catone, L. Di Mario, F. Toschi, M. Magnozzi, F. Bisio, A. Alabastri, R. Proietti Zaccaria, A. Toma, G. Della Valle, and A. Paladini, *Laser Photonics Rev.* **15**, 2100017 (2021).
- ¹⁰⁹R. Rosei, *Phys. Rev. B* **10**, 474 (1974).
- ¹¹⁰G. Della Valle, M. Conforti, S. Longhi, G. Cerullo, and D. Brida, *Phys. Rev. B* **86**, 155139 (2012).
- ¹¹¹A. Marini, M. Conforti, G. Della Valle, H. Lee, T. X. Tran, W. Chang, M. Schmidt, S. Longhi, P. S. J. Russell, and F. Biancalana, *New J. Phys.* **15**, 013033 (2013).
- ¹¹²O. Yeshchenko, I. Bondarchuk, V. Gurin, I. Dmitruk, and A. Kotko, *Surf. Sci.* **608**, 275 (2013).
- ¹¹³Y. Lu, W. Dong, Z. Chen, A. Pors, Z. Wang, and S. I. Bozhevolnyi, *Sci. Rep.* **6**, 30650 (2016).

- ¹¹⁴S. Ishii, S. L. Shinde, and T. Nagao, *Adv. Opt. Mater.* **7**, 1800603 (2019).
- ¹¹⁵T. Hong, B. Chamlagain, S. Hu, S. M. Weiss, Z. Zhou, and Y.-Q. Xu, *ACS Nano* **9**, 5357 (2015).
- ¹¹⁶M. W. Graham, S.-F. Shi, Z. Wang, D. C. Ralph, J. Park, and P. L. McEuen, *Nano Lett.* **13**, 5497 (2013).
- ¹¹⁷A. S. Kim, A. Goswami, M. Taghinejad, and W. Cai, *Proc. Natl. Acad. Sci. U.S.A.* **121**, 13 (2024).
- ¹¹⁸M. Taghinejad, H. Taghinejad, Z. Xu, Y. Liu, S. P. Rodrigues, K. T. Lee, T. Lian, A. Adibi, and W. Cai, *Adv. Mater.* **30**, 1704915 (2018).
- ¹¹⁹M. Lorenc, M. Ziolk, R. Naskrecki, J. Karolczak, J. Kubicki, and A. Maciejewski, *Appl. Phys. B: Lasers Opt.* **74**, 19 (2002).
- ¹²⁰B. Dietzek, T. Pascher, V. Sundström, and A. Yartsev, *Laser Phys. Lett.* **4**, 38 (2006).
- ¹²¹Z. Chai, X. Hu, F. Wang, X. Niu, J. Xie, and Q. Gong, *Adv. Opt. Mater.* **5**, 1600665 (2017).
- ¹²²M. Taghinejad, H. Taghinejad, Z. Xu, K.-T. Lee, S. P. Rodrigues, J. Yan, A. Adibi, T. Lian, and W. Cai, *Nano Lett.* **18**, 5544 (2018).
- ¹²³A. Schirato, M. Maiuri, A. Toma, S. Fugattini, R. Proietti Zaccaria, P. Laporta, P. Nordlander, G. Cerullo, A. Alabastri, and G. Della Valle, *Nat. Photonics* **14**, 723 (2020).
- ¹²⁴M. Taghinejad, Z. Xu, K.-T. Lee, T. Lian, and W. Cai, *Phys. Rev. Lett.* **124**, 013901 (2020).
- ¹²⁵M. Taghinejad, C. Xia, M. Hrton, K.-T. Lee, A. S. Kim, Q. Li, B. Guzelurk, R. Kalousek, F. Xu, W. Cai, A. M. Lindenberg, and M. L. Brongersma, *Science* **382**, 299 (2023).
- ¹²⁶Y. Fu, Z. Song, M. Jiang, H. Ma, R. Lopez, J. Wang, Y. Li, and X. Zhang, *ACS Photonics* **9**, 3950 (2022).
- ¹²⁷K. F. MacDonald, Z. L. Sámson, M. I. Stockman, and N. I. Zheludev, *Nat. Photonics* **3**, 55 (2009).
- ¹²⁸M. Kauranen and A. V. Zayats, *Nat. Photonics* **6**, 737 (2012).
- ¹²⁹G. Li, S. Zhang, and T. Zentgraf, *Nat. Rev. Mater.* **2**, 1 (2017).
- ¹³⁰N. Bloembergen, R. K. Chang, S. Jha, and C. Lee, *Phys. Rev.* **174**, 813 (1968).
- ¹³¹V. Mizrahi and J. E. Sipe, *J. Opt. Soc. Am. B* **5**, 660 (1988).
- ¹³²Y. Shen, *Nature* **337**, 519 (1989).
- ¹³³R. Terhune, P. Maker, and C. Savage, *Phys. Rev. Lett.* **8**, 404 (1962).
- ¹³⁴C. Lee, R. Chang, and N. Bloembergen, *Phys. Rev. Lett.* **18**, 167 (1967).
- ¹³⁵K.-T. Lee, M. Taghinejad, J. Yan, A. S. Kim, L. Raju, D. K. Brown, and W. Cai, *ACS Photonics* **6**, 2663 (2019).
- ¹³⁶H. Yu, D. Talukdar, W. Xu, J. B. Khurgin, and Q. Xiong, *Nano Lett.* **15**, 5653 (2015).
- ¹³⁷X. Wen, W. Xu, W. Zhao, J. B. Khurgin, and Q. Xiong, *Nano Lett.* **18**, 1686 (2018).
- ¹³⁸A. Schirato, A. Mazzanti, R. Proietti Zaccaria, P. Nordlander, A. Alabastri, and G. Della Valle, *Nano Lett.* **21**, 1345 (2021).
- ¹³⁹A. Block, M. Liebel, R. Yu, M. Spector, Y. Sivan, F. García de Abajo, and N. F. van Hulst, *Sci. Adv.* **5**, eaav8965 (2019).
- ¹⁴⁰Y. Sivan and M. Spector, *ACS Photonics* **7**, 1271 (2020).
- ¹⁴¹A. S. Kim, M. Taghinejad, A. Goswami, L. Raju, K. T. Lee, and W. Cai, *Adv. Sci.* **10**, 2205434 (2023).
- ¹⁴²H. Harutyunyan, A. B. Martinson, D. Rosenmann, L. K. Khorashad, L. V. Besteiro, A. O. Govorov, and G. P. Wiederrecht, *Nat. Nanotechnol.* **10**, 770 (2015).
- ¹⁴³J. Fielden, J. M. Sumliner, N. Han, Y. V. Geletii, X. Xiang, D. G. Musaev, T. Lian, and C. L. Hill, *Chem. Sci.* **6**, 5531 (2015).
- ¹⁴⁴J. D. Jackson, *Classical electrodynamics* (John Wiley & Sons, 2021).
- ¹⁴⁵E. Y. Ma, B. Guzelurk, G. Li, L. Cao, Z.-X. Shen, A. M. Lindenberg, and T. F. Heinz, *Sci. Adv.* **5**, eaau0073 (2019).
- ¹⁴⁶L. Yang, Z. An, R. Qian, H. Pan, P. Chen, W. Lu, and S. Komiyama, *ACS Photonics* **8**, 2674 (2021).
- ¹⁴⁷D. Zhang, Z. Xu, G. Cheng, Z. Liu, A. R. Gutierrez, W. Zang, T. B. Norris, and Z. Zhong, *Nat. Commun.* **13**, 6404 (2022).
- ¹⁴⁸J. Aizpurua, F. Baletto, J. Baumberg, P. Christopher, B. De Nijs, P. Deshpande, Y. Diaz Fernandez, L. Fabris, S. Freakley, S. Gawinkowski, and A. Govorov, *Faraday Discuss.* **214**, 245 (2019).
- ¹⁴⁹Y. Sivan, I. W. Un, and Y. Dubi, *Faraday Discuss.* **214**, 215 (2019).
- ¹⁵⁰J. B. Khurgin, *Nat. Nanotechnol.* **10**, 2 (2015).